Supplementary Information

Supersoft yet tough bottlebrush polymers via dynamic domain exchange

Hyunjun Kim[1†], Yeonzu Son[2†], Jaeho Lee[1†], Ji Woong Yu[3†], Intanon Lapkriengkri[4], Byeongdu Lee[5], YongJoo Kim[6*], Seongjun Park[7,8*], Christopher M. Bates[4*], and Jiheong Kang[1*]

[1] Department of Chemistry, Seoul National University, Seoul, 08826, Republic of Korea

[2] Program of Brain and Cognitive Engineering, Korea Advanced Institute of Science and Technology, Daejeon, 34141, Republic of Korea

[3] Korea Institute for Advanced Study, Seoul, 02455, Republic of Korea

[4] Materials Department, University of California, Santa Barbara, CA, 93106, USA

[5] X-ray Science Division, Advanced Photon Source, Argonne National Laboratory, Lemont, IL, 60439, USA

[6] Department of Materials Science and Engineering, Korea University, Seoul, 02841, Republic of Korea

[7] School of Transdisciplinary Innovations, Seoul National University, Seoul, 08826, Republic of Korea

[8] Medical Research Center, Seoul National University, Seoul, 03080, Republic of Korea

†These authors equally contributed to this work

*To whom correspondence should be addressed:

E-mail: jiheongkang@snu.ac.kr, cbates@ucsb.edu, seongjunpark@snu.ac.kr, cjyjee@korea.ac.kr

Materials and Methods

Materials

Unless otherwise specified, the chemicals and solvents used in the current work were purchased from Sigma-Aldrich and used without further purification. Styrene, 1-bromo-1-benzyl ethane, propargyl amine, sodium azide, 5-aminohexanoic acid, *p*-xylene, G2 Grubb's catalyst, hexane, ethyl vinyl ether, and 2-hydroxy-4'-(2-hydroxyethoxy)-2-methylpropiophenone (Irgacure 2959) were purchased from Sigma-Aldrich. Norbornene *exo*-anhydride, Polyethylene glycol monomethyl ether (M_n : 550, 4,000), diethylene glycol monoethyl ether, and *N*-(3-Dimethylaminopropyl)-*N'*-ethylcarbodiimide hydrochloride (EDC·HCl) were purchased from TCI chemicals. Monomethacrylopropyl terminated polydimethylsiloxane (MCR-M11, M_n : 1,000) and methacryloxypropyl terminated polydimethylsiloxane (DMS-R22, M_n : 10,000) were purchased from Gelest and purified using basic alumina columns to remove inhibitor. Sylgard 184 were purchased from Dow Corning. SEBS was purchased from AsahiKASEI (TUFTEC™ H1221).

General measurements

All air-sensitive manipulations were carried out under an argon atmosphere by standard Schlenk-line techniques. Dichloromethane (DCM) and tetrahydrofuran (THF) solvents were saturated with argon and purified through activated Al_2O_3 columns under argon (Chembly SPS H4). Solution ^1H NMR spectra were recorded on Bruker AVANCE III HD Nanobay (400 MHz), Bruker AVANCE III HD (400 MHz), Bruker AVANCE NEO Nanobay (400 MHz), or Bruker AVANCE NEO (500 MHz) spectrometer, and chemical shifts were referenced to the residual solvent peaks. DSC experiments were carried out with a NETZSCH DSC 214 Polyma using Concavus® pans. Transmission electron microscopo (TEM) imaging was performed with FEI company Tecnai G2 F30 S-Twin under 300 kV beam voltage.

Synthetic Protocols

Nb-COOH synthesis.

Norbornene *exo*-anhydride (1.0 equivalent, 8 g, 48.7 mmol), 6-aminohexanoic acid (1.0

equivalent, 6.39 g, 48.7 mmol), triethylamine (0.1 equivalent, 0.679 mL, 4.87 mmol), and toluene (51 mL) were combined in a round-bottom flask containing a stir bar and equipped with a Dean-Stark trap. The mixture was heated at 110 °C for 19 hours, then cooled to room temperature, and the solvent was evaporated under reduced pressure. The resulting solid was dissolved in dichloromethane, washed with water (3x), washed with brine (3x), and dried over magnesium sulfate. After removal of the solvent under vacuum, a white or slightly off-white solid was obtained.

Nb-PEG macromonomer synthesis.

Norbornene carboxylic acid imide (1.2 equivalents, 19.742 g, 71.2 mmol), poly(ethylene glycol) methyl ether (Mn=550 g/mol, 1.0 equivalent, 27.641 g, 59.3 mmol), 1-Ethyl-3-(3-dimethylaminopropyl)carbodiimide (1.6 equivalents, 18.244 g, 117.5 mmol), 4-dimethylaminopyridine (0.1 equivalent, 0.725 g, 5.9 mmol), and dichloromethane (790 mL) were combined in a 1 L round-bottom flask fitted with a stir bar. The reaction mixture was stirred for 24 hours, during which approximately half of the dichloromethane was removed under vacuum. The resulting mixture was then washed sequentially with 1 M HCl (3x), brine (1x), and dried over sodium sulfate.

After most of the solvent was removed under vacuum, the remaining solution was precipitated into diethyl ether at -78 °C. The resulting off-white solid was filtered and dried under vacuum to yield 32.3 g (93% yield) of isolated material.

Nb-propargyl imide synthesis.

Norbornene *exo*-anhydride (1.0 equivalent, 5 g, 30.4 mmol), propargylamine (1.05 equivalent, 1.76 g, 31.9 mmol), triethylamine (0.1 equivalent, 0.436 mL, 3.04 mmol), and toluene (51 mL) were combined in a round-bottom flask containing a stir bar and equipped with a Dean-Stark trap. The mixture was heated at 110 °C for 19 hours, then cooled to room temperature, and the solvent was evaporated under reduced pressure. The crude solid was recrystallized in ethanol to yield light yellow crystals.

PS-Br synthesis.

Styrene monomer (500 mL) was filtered with basic alumina to obtain a clear liquid. In a 500 mL Schlenk flask equipped with a stir bar and septum, styrene (50.0 equivalents, 350 mL, 3.054 mol) was added. The flask was then charged with N,N,N′,N′,N″-pentamethyldiethylenetriamine ligand (0.3 equivalents, 3.83 mL, 0.018 mol) and subjected to three cycles of freeze-pump-thaw to remove oxygen. After freezing in liquid nitrogen and introducing an active flow of argon, Cu(I)Br (0.3 equivalents, 2.63 g, 0.018 mol) was rapidly added upon removal of the septum. The septum was reattached, argon flow halted, and the flask evacuated.

Following three additional cycles of pump/purge with vacuum and argon, the flask was maintained under dynamic vacuum for at least 5 minutes. Thawing was conducted using warm water under an argon atmosphere. A green solution resulted, indicating partial dissolution of copper; a blue or yellow color would have indicated oxygen contamination or insufficient copper dissolution, respectively, signaling a failed polymerization attempt.

Simultaneously, 1-bromo-1-benzyl ethane was subjected to three freeze-pump-thaw cycles in a separate flask. 1-bromo-1-benzyl ethane (1.0 equivalent, 8.36 mL, 0.061 mol) was then injected into the Schlenk flask containing styrene, and the mixture was heated in an oil bath preset to 100 °C. Samples were withdrawn at intervals of approximately 30 minutes under a continuous flow of argon, and the conversion was monitored by ^{1}H NMR. Polymerization was halted after 2 hours and 35 minutes, achieving approximately 38% conversion, by quenching in liquid nitrogen.

The viscous solution was warmed to room temperature, diluted with tetrahydrofuran (100 mL), and passed through basic alumina to remove residual copper. Precipitation into methanol at -78 °C followed, yielding a polymer that was subsequently redissolved in THF and subjected to five additional precipitation cycles into methanol at -78 °C. The final product, a white powder, was obtained after drying under vacuum.

PS-N_3 synthesis.

Polystyrene (1.0 equivalent, 73 g, 37.0 mmol), sodium azide (3.0 equivalents, 7.12 g, 109.5 mmol), and dimethylformamide (350 mL) were combined in a round-bottom flask equipped with a stir bar and reflux condenser. The mixture was heated at 65 °C for 16 hours, then cooled to room temperature. The resulting product was precipitated into methanol at -78 °C. After precipitation, the solid was redissolved in tetrahydrofuran (THF), and this precipitation process was repeated four additional times.

Nb-PS macromonomer synthesis.

Polystyrene-azide (1.0 equivalent, 64.30 g, 30.6 mmol), norbornene propargyl imide (1.5 equivalents, 9.24 g, 45.9 mmol), and Cu(I)Br (0.4 equivalent, 1.76 g, 12.3 mmol) were introduced into a 500 mL three-neck round-bottom flask equipped with a stir bar, reflux condenser, and two septa. The flask underwent three cycles of pump/purge with argon and was subsequently placed under an argon atmosphere. Dry tetrahydrofuran (180 mL) was added using a syringe, followed by N,N,N′,N′,N″-pentamethyldiethylenetriamine (0.4 equivalent, 2.56 mL, 12.3 mmol), resulting in a light green and clear solution.

The reaction mixture was heated at 50 °C for 16 hours and then allowed to cool to room temperature. It was then diluted with tetrahydrofuran (100 mL), filtered through basic alumina to remove copper residues, and precipitated into methanol at -78 °C. This precipitation process was repeated five additional times to yield a white powder.

Preparation of reconstructive BBP elastomer bulk film

Bulk BBP film was prepared by the solvent casting. 1.5 g of synthesized triblock bottle brush polymer was dissolved in 60 mL of chloroform and the solution was cast into a Teflon mold. The ambient conditions allowed for the complete evaporation of the solvent. Subsequently, to remove any residual solvent, the casting was subjected to overnight drying at 50℃ in a vacuum oven. All the elastomer films for analysis and applications were prepared in the same way.

Preparation of chemically crosslinked BBP network film

In a glove box, PDMS-acrylate macromonomer (MCR-M11, 1.0 equivalent, 1 g, 1 mmol), PDMS-diacrylate crosslinker (DMS-R22, 0.1 equivalent, 1 g, 0.1 mmol) and 1.5 wt% of photoinitiator (Irgacure 2595, 45 mg) were dissolved in 1 mL of *p*-xylene and stirred in a 10 mL glass vial. The mixture was poured onto a 65 mm Teflon mold and cured using a 40 W 365 nm UV lamp (VILBER, Bio-Link) for 10 hours. Films were washed with chloroform (2x) in glass petri dishes for 8 hours. The film was then deswelled with ethanol and dried in a 50 ℃ vacuum oven.

Coarse-grained model simulation (CGMS)

Calculation of normalized squared end-to-end distance

The configuration of each polymer is quantitatively represented by the end-to-end distance, R_{e}. To compensate for the length effect, we normalize the end-to-end squared distance by the squared end-to-end distance of a freely jointed chain (FJC). This introduces a new parameter, $\kappa_{\mathrm{FJC}}^{\alpha}$, which is the normalized end-to-end squared distance (see Equation (1)).

$$\kappa_{\mathrm{FJC}} = \frac{\langle R_{\mathrm{e}}^{2} \rangle}{nb^{2}} \tag{1}$$

Here, n represents $n = N - 1$, where N is the number of monomers in the backbone, and b is the bond length, which corresponds to the minimum point in the FENE bond.

Calculation of nematic order parameter

The nematic order parameter, S_{x}^{α}, is calculated at each sampled strain (see equation (2)). The calculation is performed on backbone segments in each block ($\alpha = \mathrm{A}, \mathrm{B}$), and the A blocks are treated as statistically equivalent because they are symmetric.

$$S_{x}^{\alpha} = \frac{3}{2} \langle \cos \theta_{\alpha,x} \rangle - 1 \tag{2}$$

Here, $\theta_{\alpha,x}$ denotes the inner product between the bond vector in the α block and the x-axis, and $\langle \cdots \rangle$ represents averaging over all bonds. The nematic order parameter measures how strongly a polymer segment aligns with a chosen axis. In this work the axis is the uniaxial deformation direction x.

Biological analysis

Histological analysis

For immunohistochemical evaluation of intraneural implants, sciatic nerves were dissected after 2-week implantation and fixed overnight in 4% paraformaldehyde at 4 °C. For cryoprotection, brains were immersed in 30% sucrose solution for a few days until fully equilibrated. The nerves were then embedded in OCT compound (Tissue-Tek, Sakura) and froze at -20 °C. Transverse sections (10µm thick) were thaw-mounted and dried for 30 minutes at 37 °C. The slide-mounted sections were rinsed in PBS prior to staining. For blocking of non-specific binding and permeabilization, the sections were incubated in 0.3% Triton-X 100 (Sigma Aldrich) and 5% Normal Donkey Serum (Abcam) solution for 1h. The sections were then incubated overnight at room temperature with primary antibodies; rabbit anti-neurofilament-200 (NF200) (ab8135, Abcam) 1:1000, goat anti-Iba1 (ab107159, Abcam) 1:500. The sections were rinsed with PBS and incubated for 1h with secondary antibodies; donkey anti-rabbit Alexa Fluor 488 (ab150064, Abcam) 1:500, donkey anti-goat IgG Alexa Fluor 647 (ab150131, Abcam) 1:500. After rinsing, the sections were counterstained with 4'6-diamidino-2-phenylindole (DAPI) (Vectashield H-1200, Vector Laboratories). The sections were imaged with a laser-scanning confocal microscope (AX, Nikon). Acquired images were analyzed with ImageJ software. A 150 μm-wide band region surrounding the polymer intraneural implant trace was analyzed. Average intensities of NF200 and Iba1 expressions were normalized to the average intensity of DAPI.

For histological evaluation of subcutaneous implants, skin samples harvested after 2-week implantation were fixed in 10% formalin for 24h before paraffin-embedding. The paraffin-embedded fixed samples were sliced (thickness 4 μm) and prepared into slides. The sections were deparaffinized and stained with hematoxylin and eosin (H&E) and Masson's trichrome.

Toe spreading reflex

The spread of hind paw in response to a startle response was observed to assess the sciatic nerve damage. The rats were suspended by their tails and lightly lifted with their noses pointing downwards[1,2]. The digit abduction in the experimental hindlimb with intraneural implant were evaluated while normal digit abduction responses were observed in non-operative hindlimb.

Gait analysis

Gait analysis was performed with CatWalk XT (Noldus Information Technology) to assess sciatic nerve functions following 2-week intraneural implantation in the sciatic nerve. Prior to evaluation, the rats were accustomed to the walking track (5-cm width) to complete the uninterrupted runs. Each rat was placed on the walkaway repeatedly at intervals of at least 5 minutes to complete three uninterrupted runs for analysis. Three runs showing four step cycles each were analyzed for each animal[3]. Functional loss of sciatic nerves was evaluated with toe spreading[4], sciatic functional index[4–6], and swing speed[3,7]. Normalized toe spread and swing speed are calculated as follows:

$$\text{Normalized toe spread} = \frac{\mathrm{ETS}}{\mathrm{NTS}}$$

(ETS=experimental toe spread; NTS=normal toe spread)

$$\text{Normalized swing speed} = \frac{\mathrm{ESP}}{\mathrm{N}SP}$$

(ESP=experimental swing speed, NSP=normal swing speed)

The footprint analysis was conducted with imageJ for measurements of following parameters. (1) distance from the heel to the third toe, the print length; (2) distance from the first to the fifth toe, the toe spread; and (3) distance from the second to the fourth toe, the intermediary toe spread. All three measurements were taken from the experimental and normal hindlimb footprints to calculate sciatic functional indices (SFI) as follows:

$$\text{SFI} = -37.2\left(\frac{EPL-NPL}{NPL}\right) + 104.4\left(\frac{ETS-NTS}{NTS}\right) + 45.6\left(\frac{EIT-NIT}{NIT}\right) - 8.8$$

(EPL = experimental print length, NPL = normal print length,
ETS = experimental toe spread, NPS = normal toe spread,
EIT = experimental intermediary toe spread, NIT = normal intermediary toe spread)
8-week female Sprague Dawley rats (Koatech) were used as the healthy control group with normal gait.

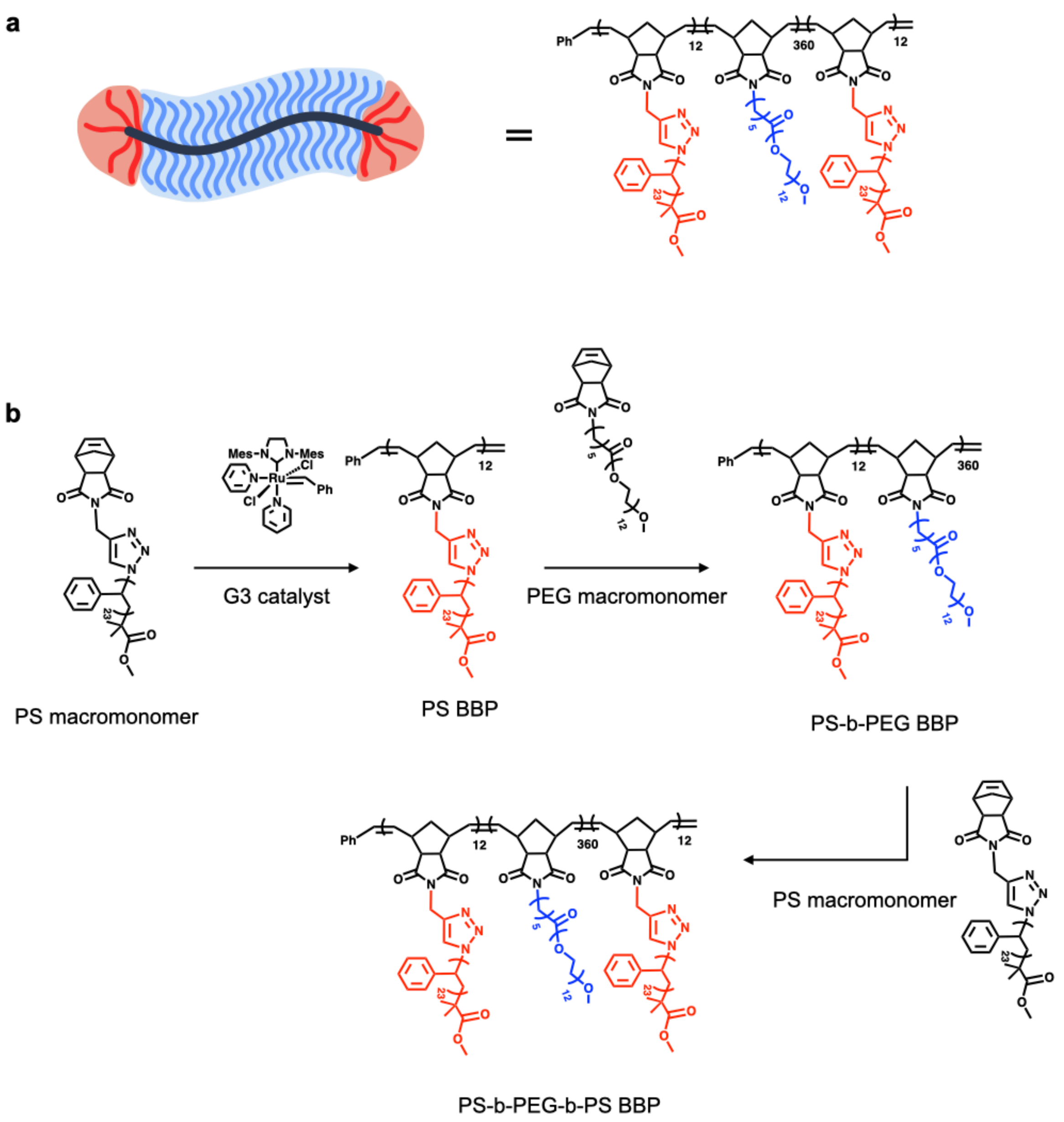

Supplementary Fig. 1 | Structure and synthetic scheme of the triblock BBP. a, Molecular structure of the triblock BBP. **b,** Synthetic scheme of the triblock BBP via ring opening metathesis polymerization (ROMP).

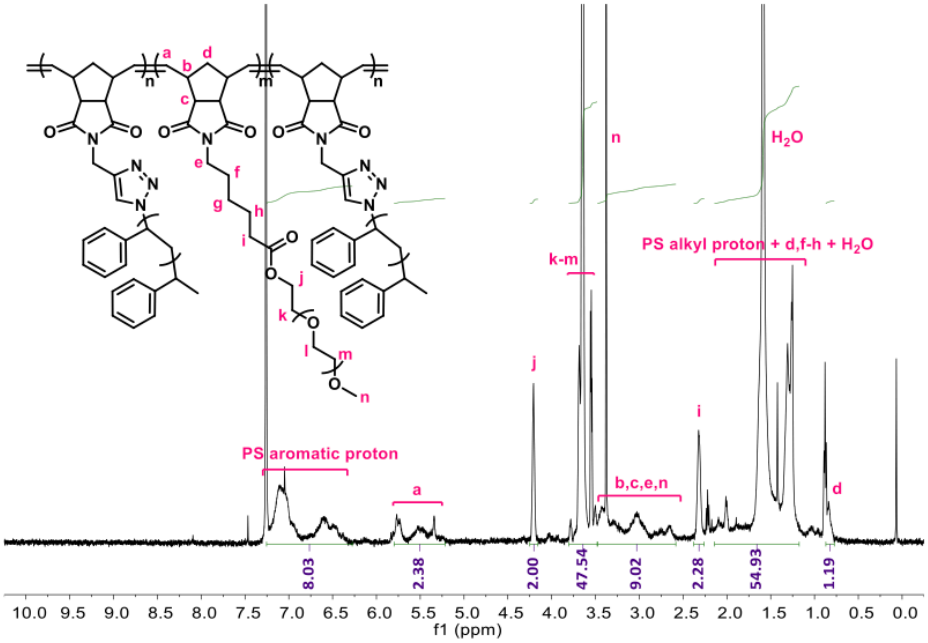

Supplementary Fig. 2 | NMR spectrum of triblock BBP. ^{1}H NMR spectrum of triblock BBP measured in $CDCl_3$ (500 MHz).

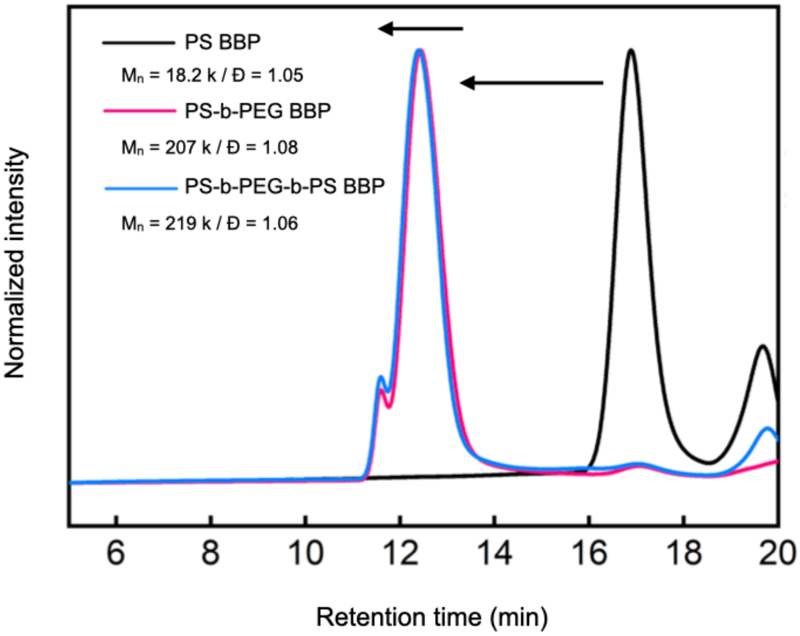

Supplementary Fig. 3 | GPC traces of triblock BBP. GPC traces (THF column) for each step of the triblock BBP synthesis. The molecular weight increases step by step and each block exhibits a narrow molecular weight distribution.

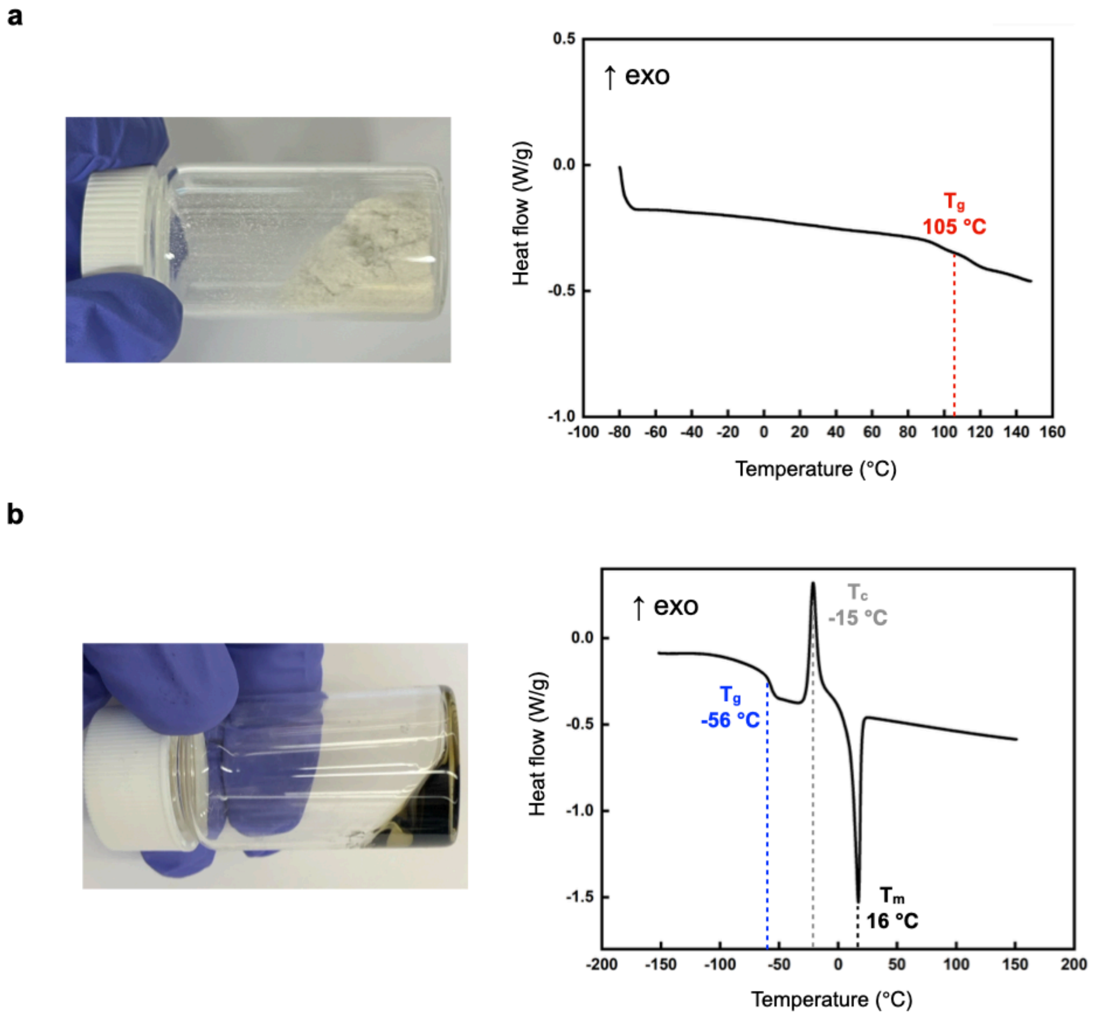

Supplementary Fig. 4 | Macroscopic mechanical properties of triblock BBP components. Bulk state images at room temperature and DSC profiles (second cycle heating) of **a,** PS homo-BBP and **b,** PEG homo-BBP. Due to the glassy nature of PS BBP and the viscous liquid behavior of PEG BBP at RT, neither system can exhibit elastomeric properties on its own.

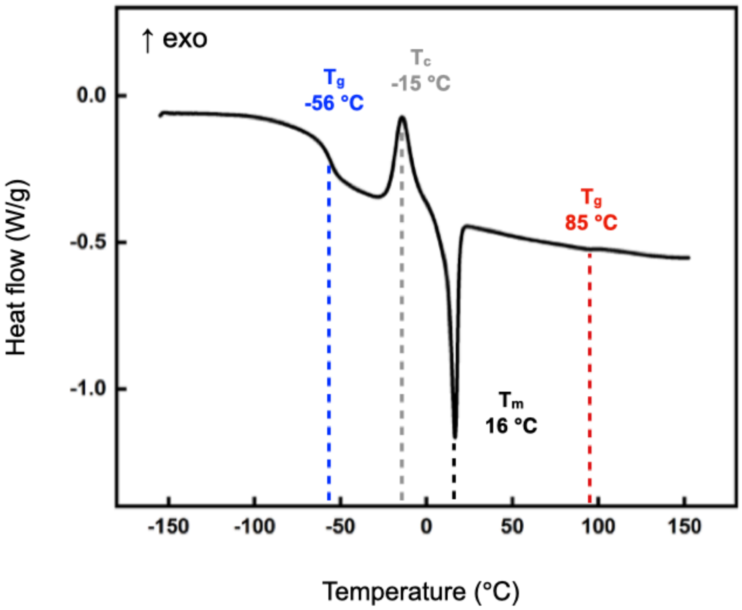

Supplementary Fig. 5 | DSC profile of the PS-*b*-PEG-*b*-PS triblock BBP. The triblock BBP incorporates the thermomechanical characteristics of the PS BBP and PEG BBP blocks. As a result, the BBP network exhibits elastomeric behavior arising from a rubbery matrix supported by glassy crosslinking domains.

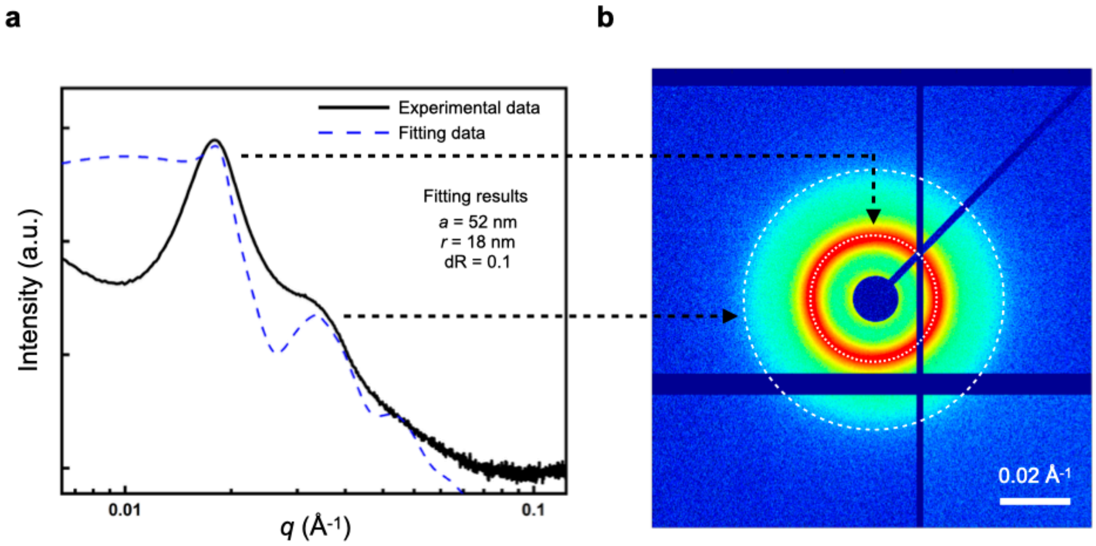

Supplementary Fig. 6 | SAXS analysis of the PS-*b*-PEG-*b*-PS triblock BBP network. a, 1D SAXS profile and **b,** 2D SAXS image. By fitting the 1D data with a BCC-sphere model[8], the inter-domain distance ***a*** and the domain radius ***r*** were determined. The surface-to-surface distance between domains (***d***) was calculated as ***a*** **-** 2***r***.

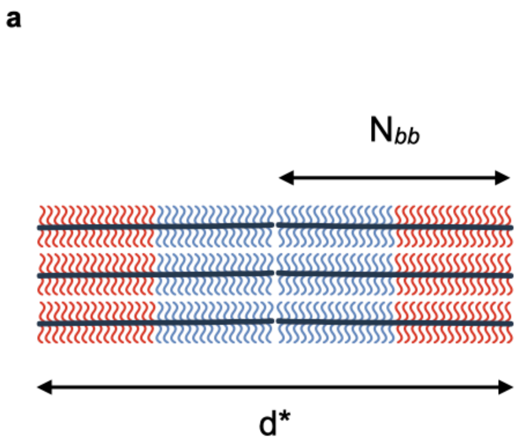

b

$$d^* \sim N_{bb}^{\alpha}$$
$$= 1.303 \times N_{bb}^{0.858}$$

α : scaling factor

Length of N_{bb} 360 PEG BBP backbone

$= d^* / 4 = 1.303 \times 720^{0.858} / 4 = 92$ nm

N_{bb}	Backbone length (nm)
200	55
360	92
800	180

Supplementary Fig. 7 | Calculation of the PEG BBP backbone length. a, Schematic illustration of the diblock copolymer BBP system used to calculate the backbone length based on the scaling law[9]. For estimating the stretched backbone length, we assume a diblock copolymer forming a lamellar structure. **b,** Scaling law and calculated backbone length as a function of the backbone DP (N_{bb}). For the diblock BBP system with a grafting density of 1, the scaling factor is 0.858.

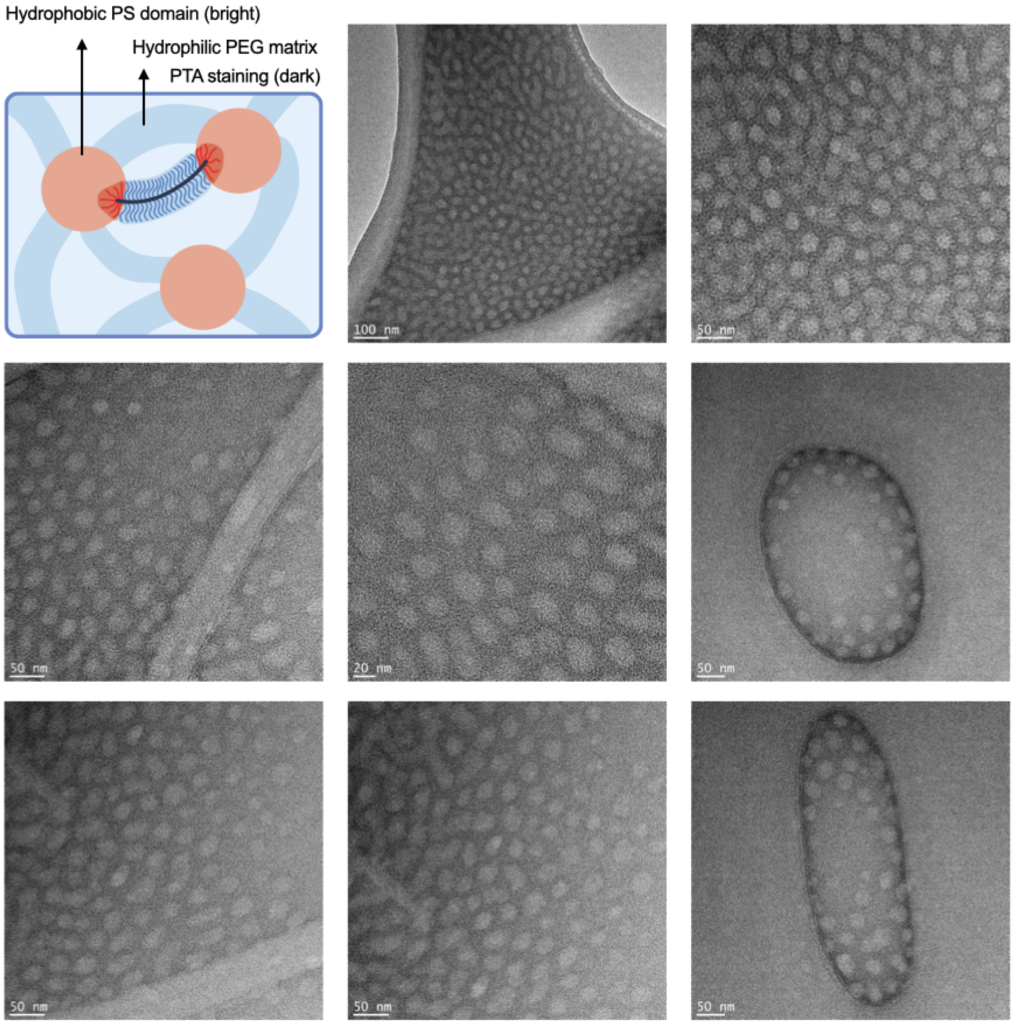

Supplementary Fig. 8 | TEM images of the triblock BBP network. The network morphology determined by SAXS analysis is further confirmed by TEM imaging. To enhance contrast, phosphotungstic acid hydrate (PTA) staining was applied, resulting in the PEG matrix dark while the unstained PS domains appear bright. The domain size (***r*** = 18 nm) and inter-domain distance (***d*** = 16 nm) obtained from SAXS are consistent with the TEM images.

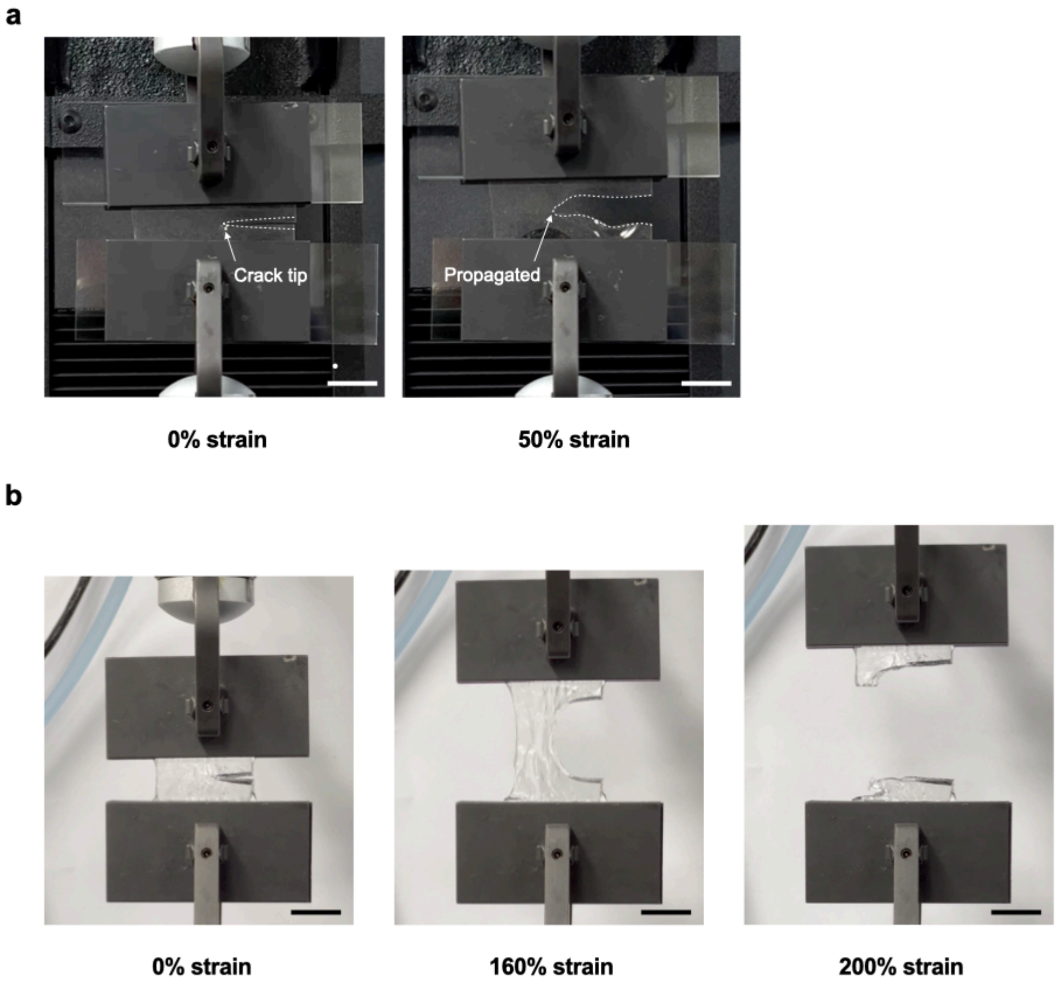

Supplementary Fig. 9 | Crack sensitivity and low fracture toughness of elastomers. Photographs of notched samples of **a,** linear PDMS elastomer and **b,** chemically crosslinked BBP network under tensile loading. Both systems lack energy dissipating or stress deconcentrating mechanisms, causing stress to concentrate at the crack tip and leading to rapid crack propagation and failure. Polymer films were prepared and notched to half of their width. Scale bars, 2 cm.

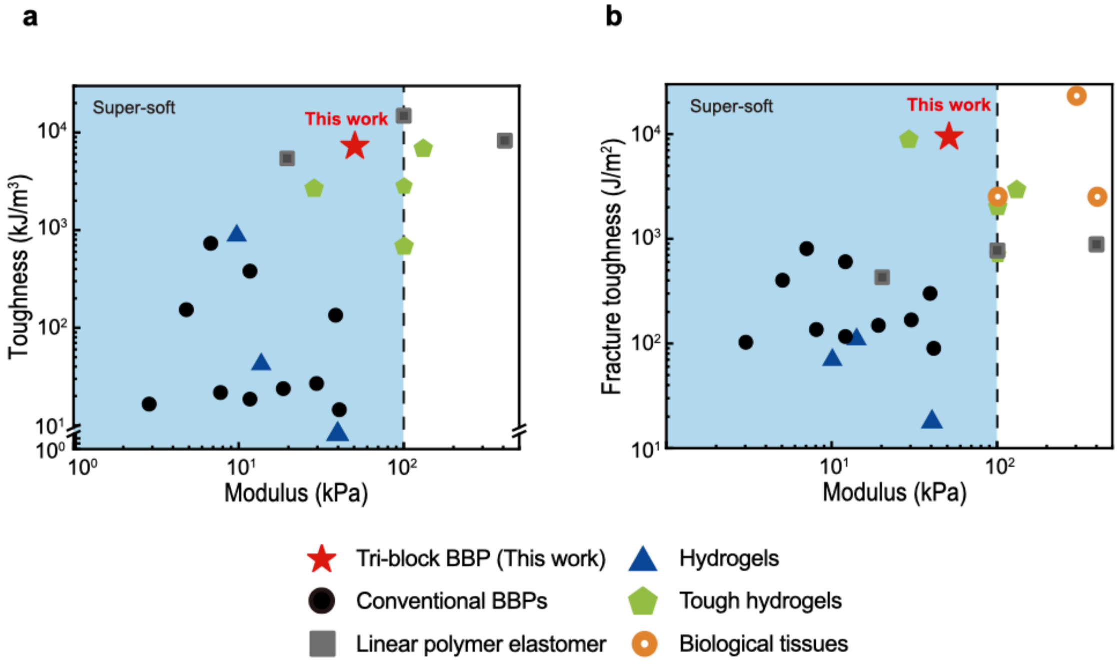

Supplementary Fig. 10 | Comparison of mechanical properties of soft polymer networks. Comparison of softness (modulus) versus **a,** toughness and **b,** fracture toughness across soft polymer systems (E < 300 kPa). Among networks with supersoftness (E < 100 kPa), the triblock BBP network exhibits record-high toughness and fracture toughness. Some linear polymers show high toughness but suffer from low fracture toughness and high modulus. The BBP network uniquely combines tissue-like softness with exceptional toughness and crack resistance. Conventional BBPs[10], Hydrogels[11], Tough hydrogels[12–15], Biological tissues[11]. Linear polymer elastomers (Ecoflex, Dragon skin, Sylgard 184) and conventional BBP (chemically crosslinked PDMS BBP) are measured.

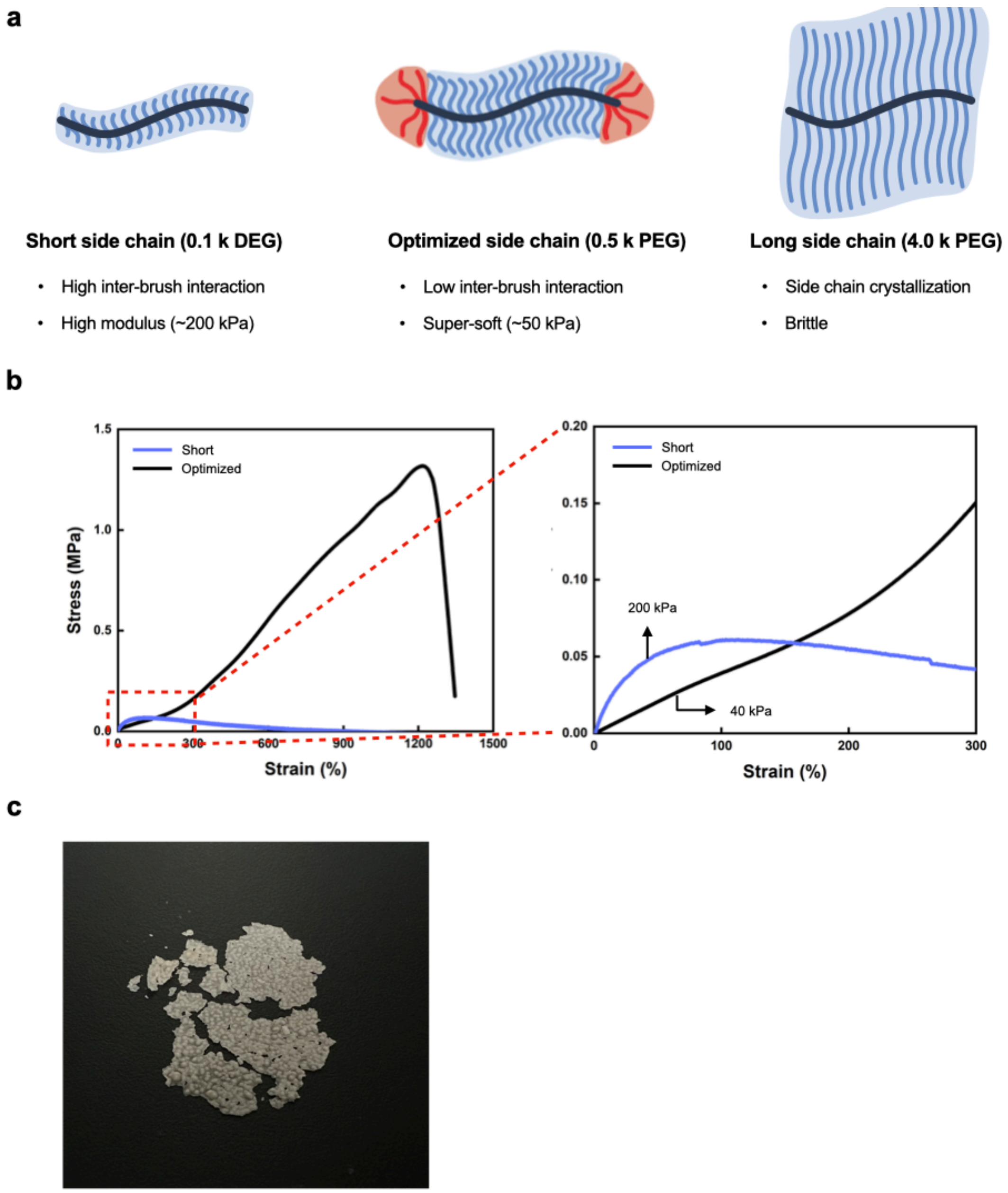

Supplementary Fig. 11 | Effect of side chain length on mechanical properties. a, To achieve supersoftness in BBP networks, we systematically investigated the influence of side chain length on modulus. Homo-BBPs with short (0.1 k DEG) and long (4.0 k PEG) side chains were synthesized and compared to BBP network with an optimized side chain length (0.5 k PEG). **b,** Uniaxial tensile testing of short side chain homo-BBP and optimized triblock BBP networks. Increased inter-brush interactions and entanglements in short side chain BBPs allow the formation of a free-standing film without glassy crosslinking domains, resulting in a higher modulus than the optimized triblock BBP network and high viscoelasticity. **c,** Photograph of the long side chain homo-BBP. The long side chain homo-BBP exhibits brittle behavior due to crystallization of the PEG side chains at room temperature.

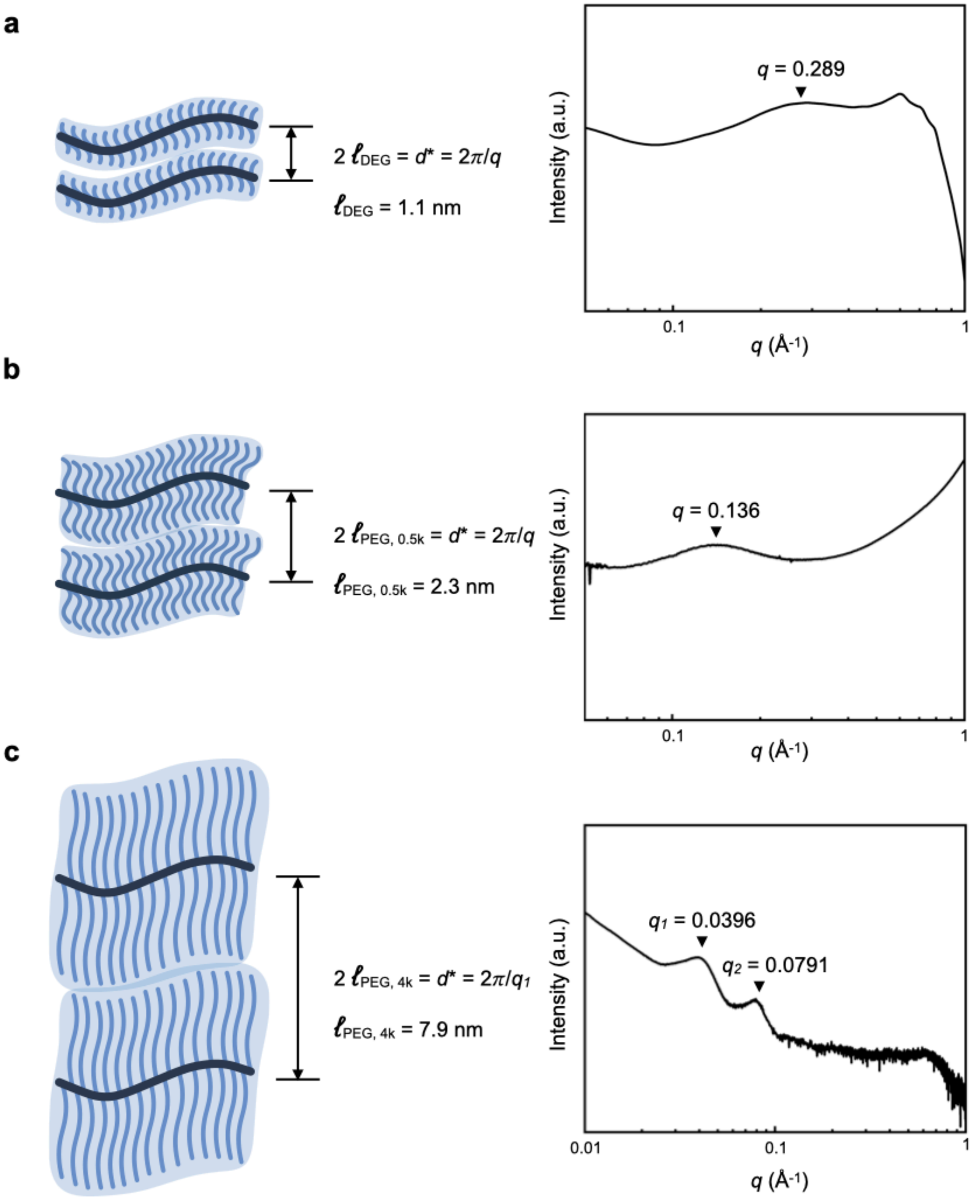

Supplementary Fig. 12 | Measurement of side chain length of BBPs. Side chain length of the BBPs are measured by the X-ray analysis. **a,** Side chain length of shorter side chain BBPs. **b,** Side chain length of optimized BBPs. **c,** Side chain length of longer side chain BBPs.

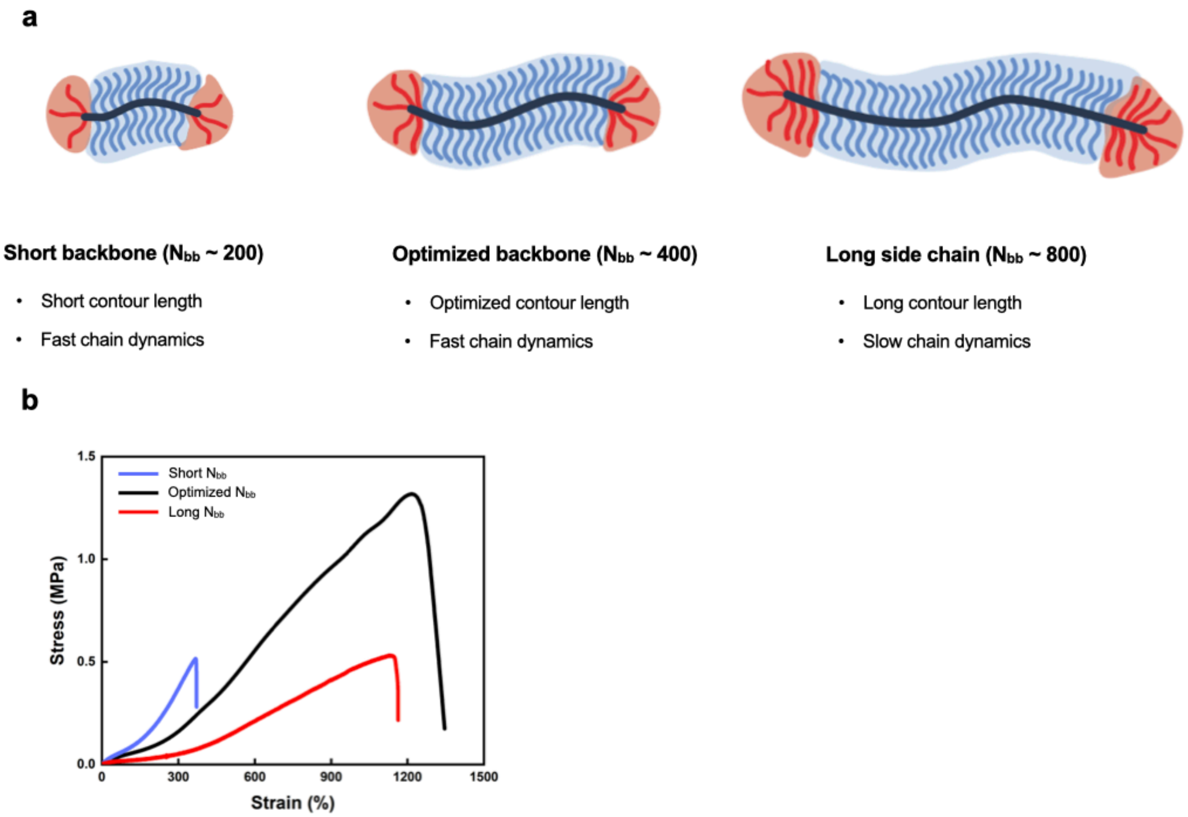

Supplementary Fig. 13 | Effect of backbone length on mechanical properties. a, To achieve supersoftness and toughness in BBP networks, we systematically investigated the effect of backbone length on stretching behavior by synthesizing triblock BBPs with short and long backbones. **b,** Uniaxial tensile testing of triblock BBP networks with the three different backbone lengths. Because backbone length governs the bending stiffness of BBPs, shorter backbone BBPs exhibit higher stiffness. In addition, the stretchability of triblock BBP system is governed by contour length and chain dynamics: short backbone BBPs show limited stretchability due to their short contour length. In contrast, long backbone BBPs exhibit moderate stretchability despite their long contour length, and reduced fracture strength attributed to slow chain dynamics.

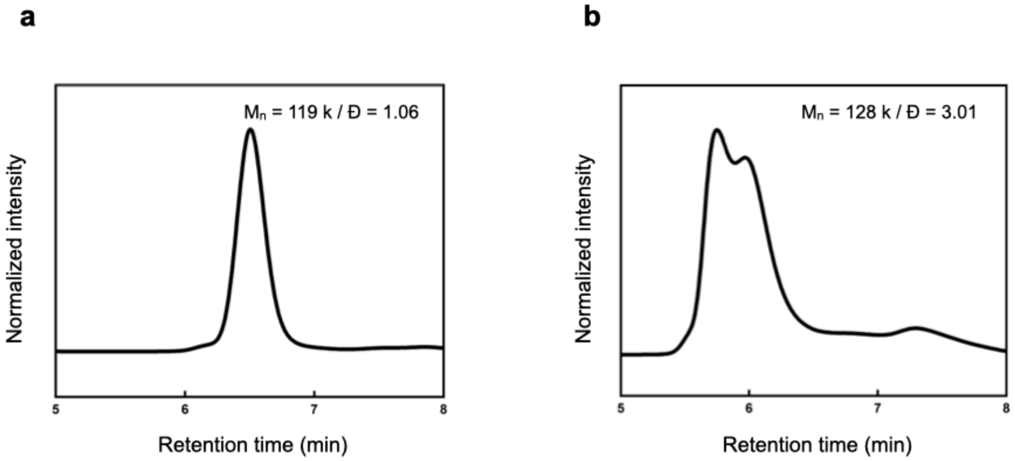

Supplementary Fig. 14 | Molecular weight distribution of short and long backbone triblock BBPs. GPC traces (THF column) of **a,** short backbone BBPs and **b,** long backbone BBPs. The short backbone BBPs exhibit a narrow molecular weight distribution comparable to that of the optimized BBP system. In contrast, the long backbone BBPs show a broader molecular weight distribution, which arises from reduced reactivity as backbone length increases. Based on the molecular weight distribution, the optimal backbone length (N_{bb}) was determined to be approximately 400.

a

Color	PS-b-PEG-b-PS N_{bb} / Mw	PS vol% (d_{PS} = 1.00 d_{PEG} = 1.15)	Young's modulus	Structure
🟦	6-360-6 17k-296k-17k	11%	40 kPa	Sphere
🟥	12-360-12 33k-296k-33k	20%	40 kPa	Sphere
🟦	18-360-18 45k-296k-50k	28%	130 kPa	Granule
🟩	24-360-24 67k-296k-67k	34%	700 kPa	Cylinder
🟪	36-360-36 100k-296k-100k	43%	3 MPa	Percolated
⬛	48-360-48 133k-296k-133k	50%	35 MPa	Lamella

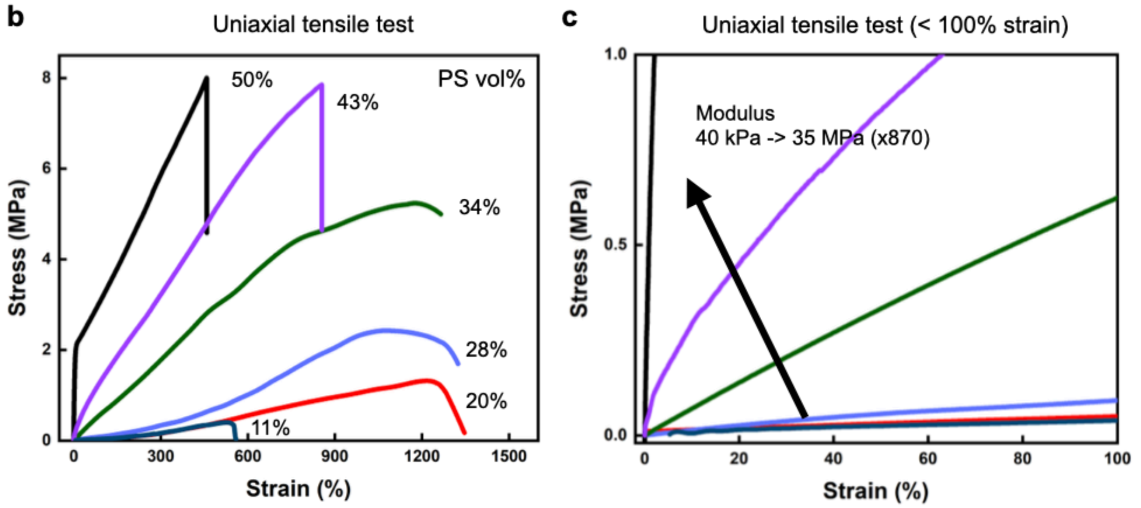

Supplementary Fig. 15 | Series of triblock BBPs with varying PS volume fractions. To investigate how microphase separated morphology influences mechanical properties, a series of BBPs was synthesized in which the PEG middle block was kept constant while the volume fraction of the PS end blocks was systematically varied. **a,** Table summarizing the BBP series and their properties **b,** Uniaxial tensile testing of the BBP series and **c,** enlarged view of the initial strain region (<100% strain) used to determine the young's modulus. As the morphology transitions from discrete spherical PS domains to a percolating network of glassy PS phases, the modulus increases dramatically. By simply increasing PS volume fraction, the modulus increases by up to 870 fold within the system. Notably, all BBP networks—regardless of morphology—exhibit high toughness.

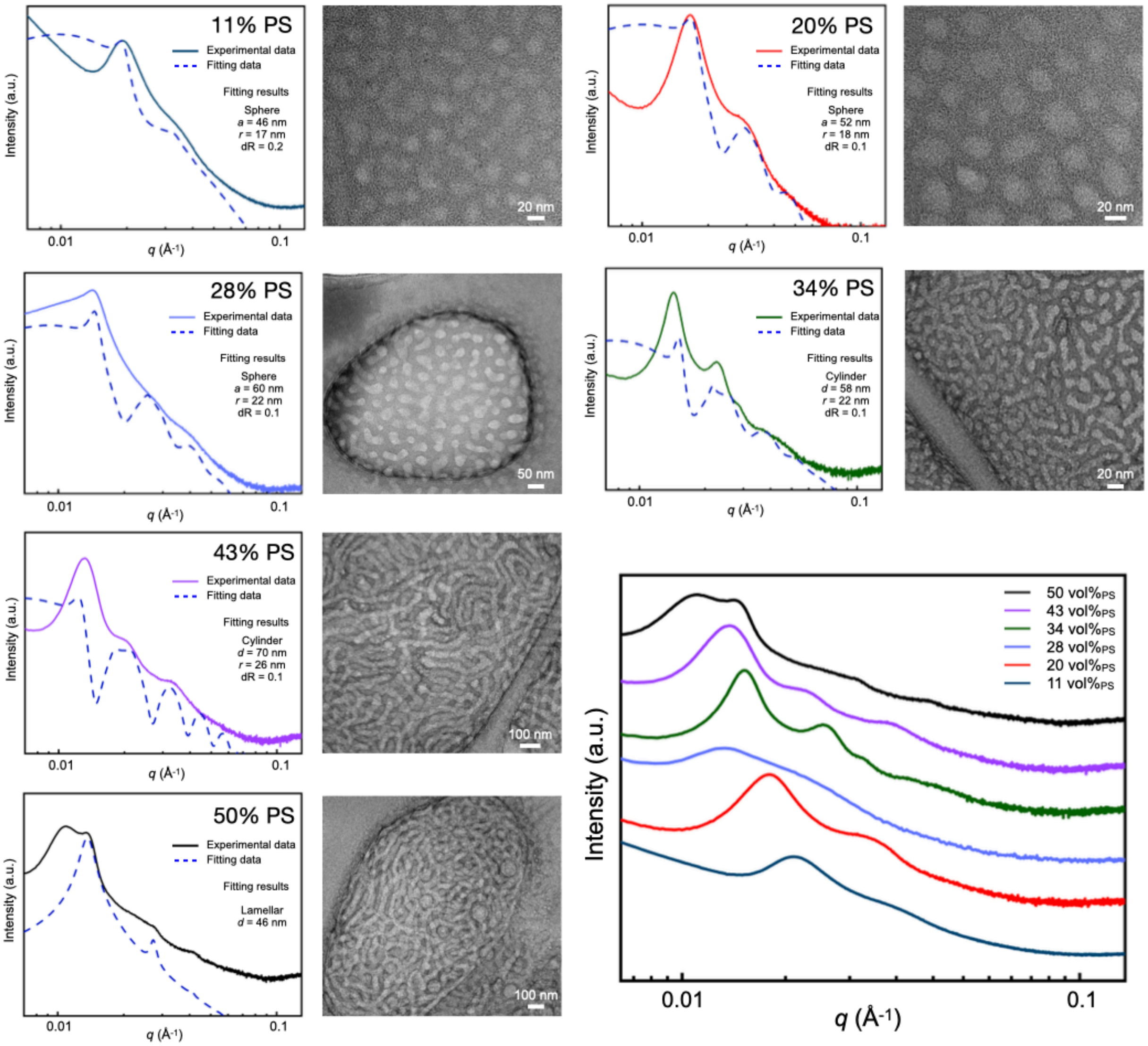

Supplementary Fig. 16 | Microphase morphology of the BBP series. As the volume fraction of the PS end blocks increases, the microphase separated morphology transitions from dispersed spherical PS domains to a percolated PS network.

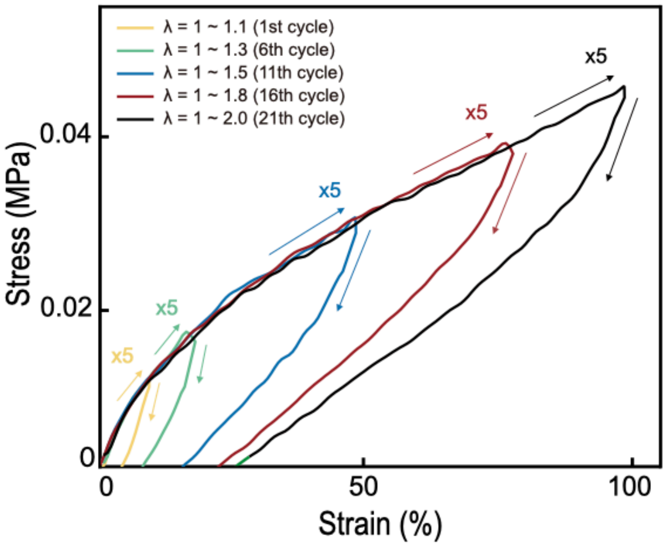

Supplementary Fig. 17 | Elasticity of triblock BBP networks. The stress-strain curves of the triblock BBP network obtained from cyclic tensile tests (10%, 30%, 50%, 80%, and 100% strain). Each cyclic test was repeated five times with a 10 seconds rest between cycles. In the loading curves, all cycles show nearly identical stress-strain behavior regardless of cycle number or strains, with no noticeable hysteresis or residual strain.

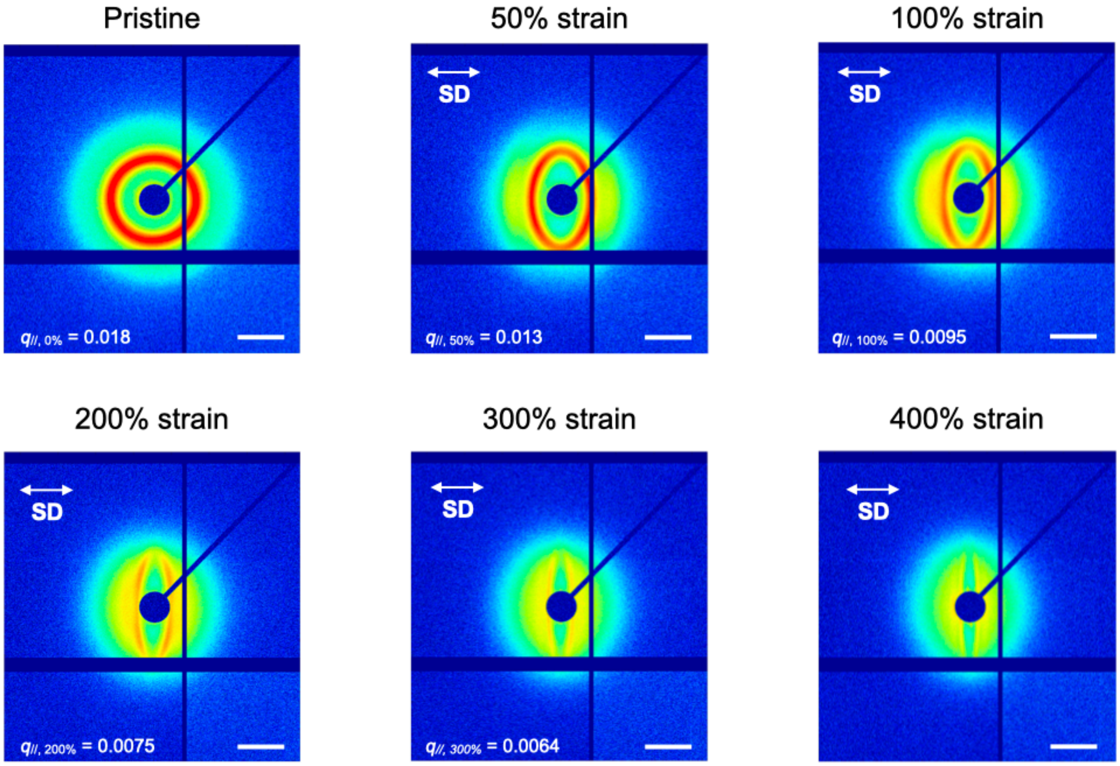

Supplementary Fig. 18 | *In-situ* stretching SAXS. 2D SAXS images collected during uniaxial stretching of the BBP network. The isotropic ring pattern progressively deforms with increasing strain. Up to 100% strain, the scattering vector along the stretching direction ($q_{//}$) decreases proportionally, while above 200% strain the decrease becomes non-proportional. This behavior indicates affine deformation of network in the low strain region and non-affine deformation at high strain region. Scale bars, 0.02 Å^{-1}.

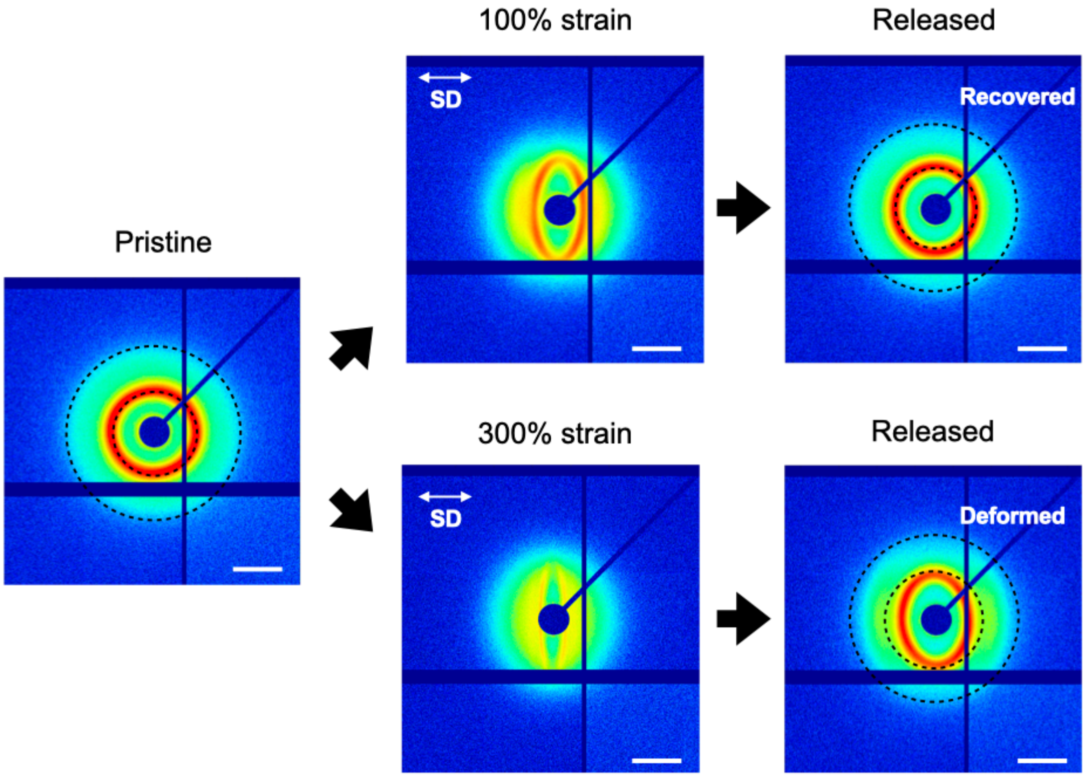

Supplementary Fig. 19 | *In-situ* stretching and recovery SAXS. 2D SAXS images obtained during cyclic loading-unloading of BBP network at 100% and 300% strain. After cycling at 100% strain, both the structural factor and form factor fully recover to their original states. In contrast, cycling at 300% strain results in incomplete recovery due to domain exchange and network reconstruction. Scale bars, 0.02 Å^{-1}.

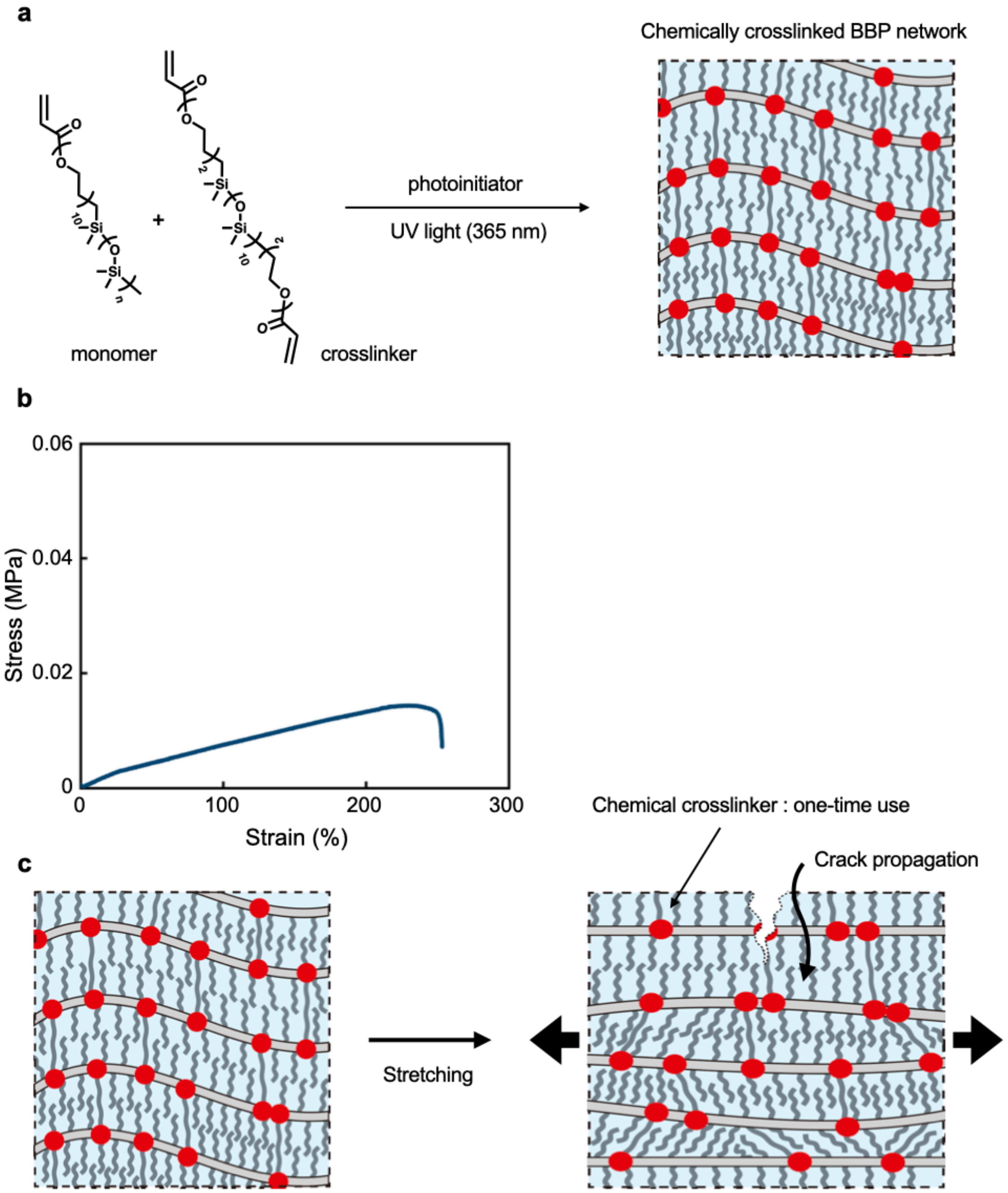

Supplementary Fig. 20 | Mechanical properties of chemically crosslinked BBP. a, Synthetic scheme of a conventional chemically crosslinked BBP network and a schematic illustration of its network architecture. The network was formed by the free-radical polymerization of acrylate based macromonomers and crosslinkers under UV irradiation. **b,** Stress-strain curve of the chemically crosslinked BBP network. **c,** Under strain, the network backbone stretches until reaching full extension. However, due to the absence of stress dissipating motifs, the crosslinkers fail. This irreversible crosslink breakage leads to rapid crack propagation and low stretchability.

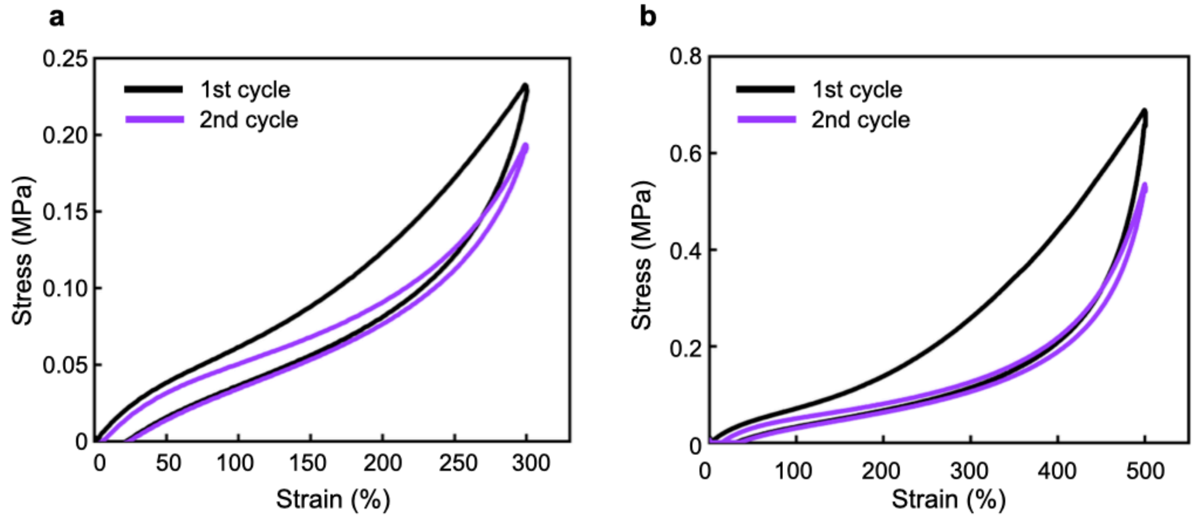

Supplementary Fig. 21 | Elasticity of triblock BBP networks at high strain. Stress-strain curves from cyclic tensile tests at **a,** 300% strain and **b,** 500% strain. In these large strain regions, the second loading cycle no longer follows the first loading curve due to plastic behavior associated with network reconstruction. Nevertheless, the residual strain remains low (30% at 300% strain and 50% at 500% strain) and is consistent across cycles.

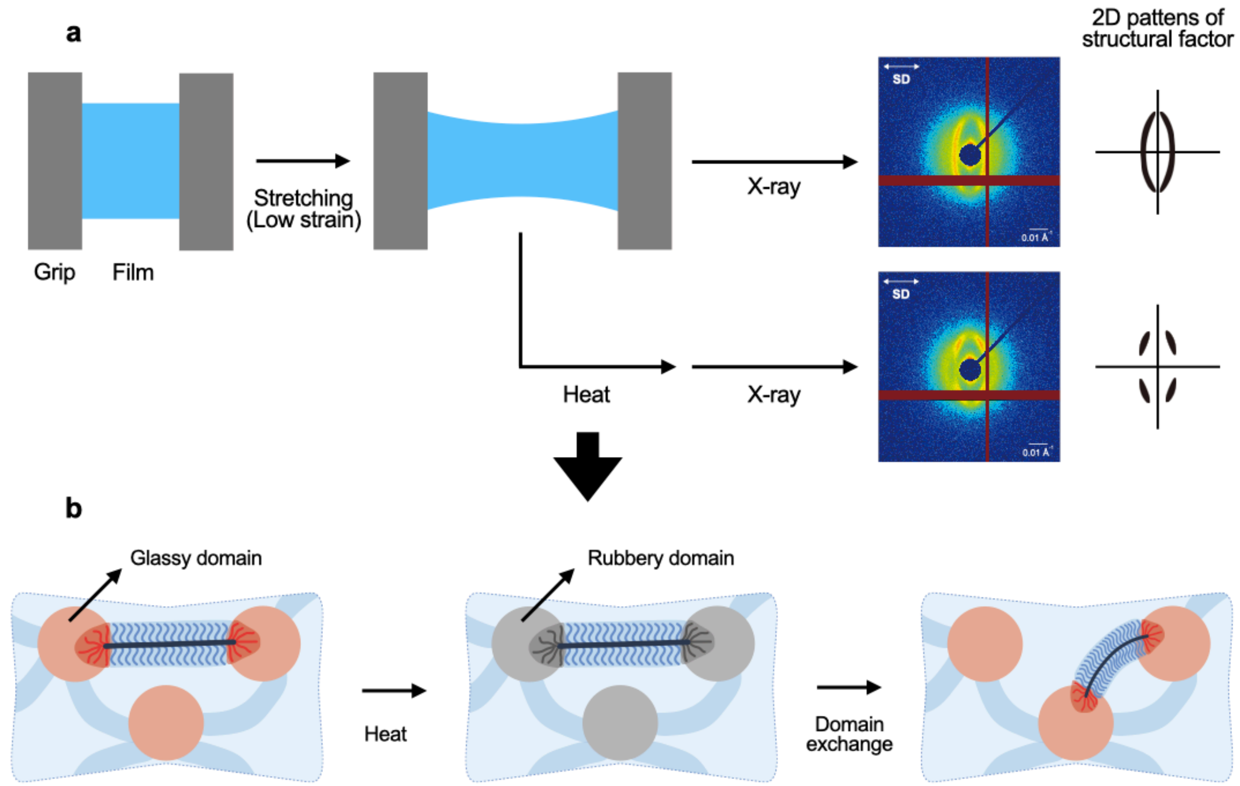

Supplementary Fig. 22 | Validating network reconstruction through structural analysis. Schematic illustration of **a,** the experimental procedure for applying thermal stimuli to stretched samples and corresponding SAXS measurements, and **b,** the network reconstruction mechanism. At small strains (< 200%), BBP backbones stretched without disrupting crosslinking domains. Upon heating, the glassy domains become rubbery and cannot sustain the stored tensile stress, resulting in domain exchange and network reconstruction. These are confirmed by characteristic changes in 2D SAXS patterns.

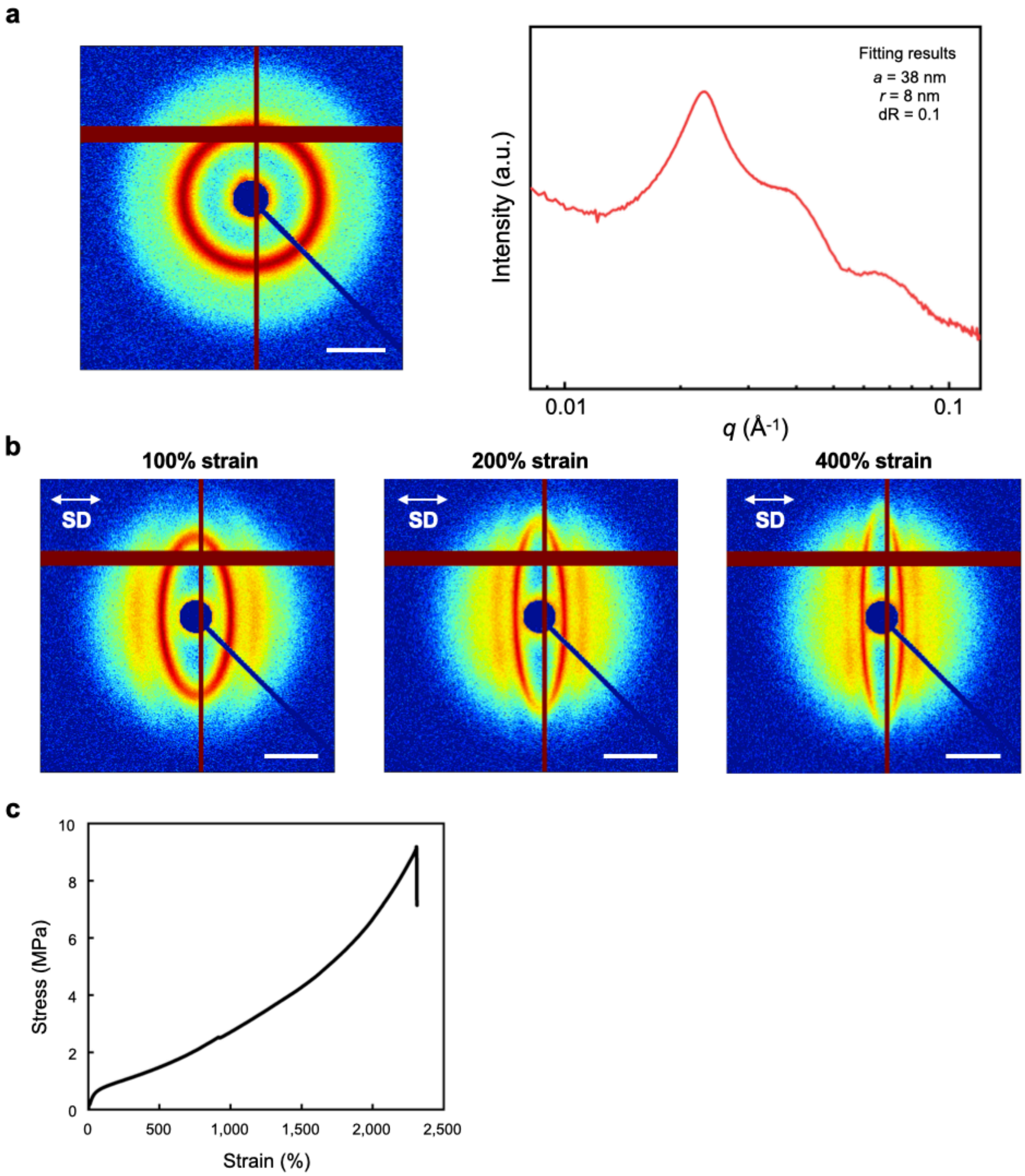

Supplementary Fig. 23 | Network structure and mechanical behavior of sphere domain SEBS. **a,** Linear triblock copolymer SEBS with 12 vol% PS exhibits spherical microdomains like those in the triblock BBP network. **b,** Upon stretch, the SEBS network shows domain deformation trends comparable to the BBP network, with isotropic ring patterns progressively distorting as strain increases. Scale bars, 0.02 $Å^{-1}$. **c,** Uniaxial tensile testing of the SEBS network shows extremely high toughness in the absence of thermal stimulation.

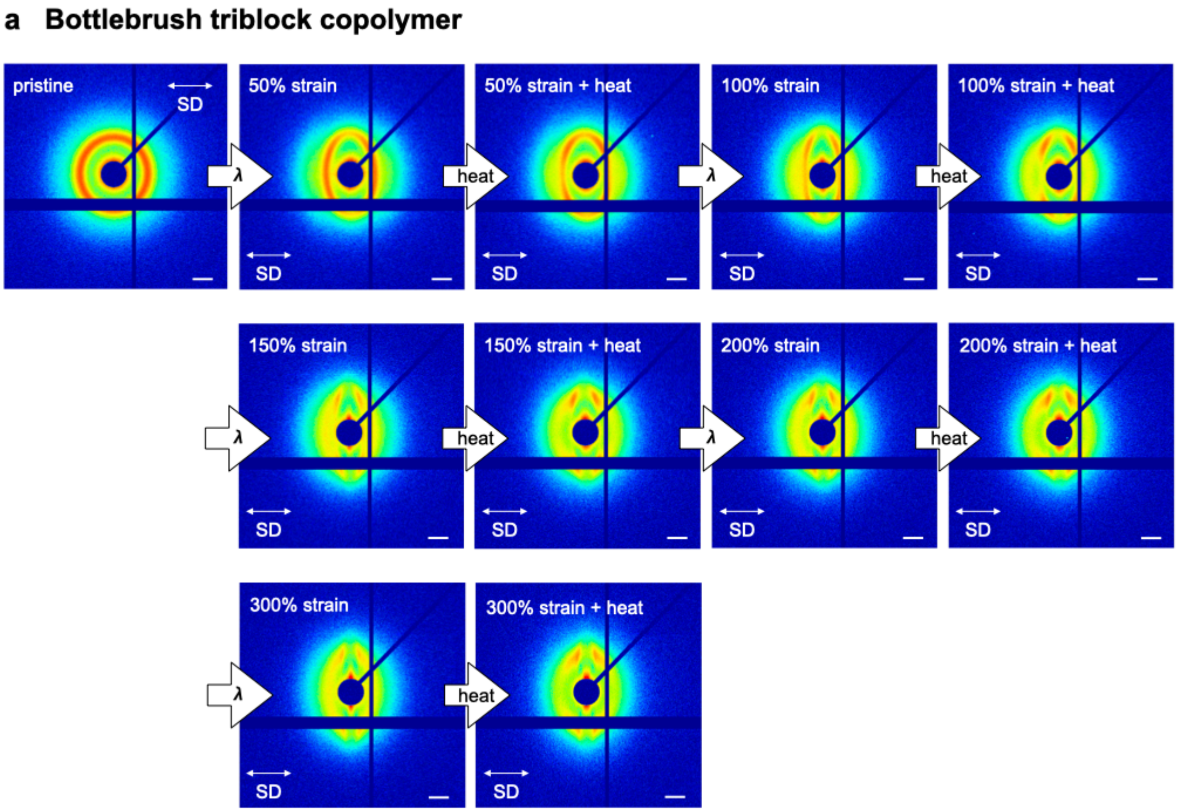

- Continuous domain exchange and network reconstruction of triblock BBP network
- Stable network at high strain (> 300% strain) under thermal stress

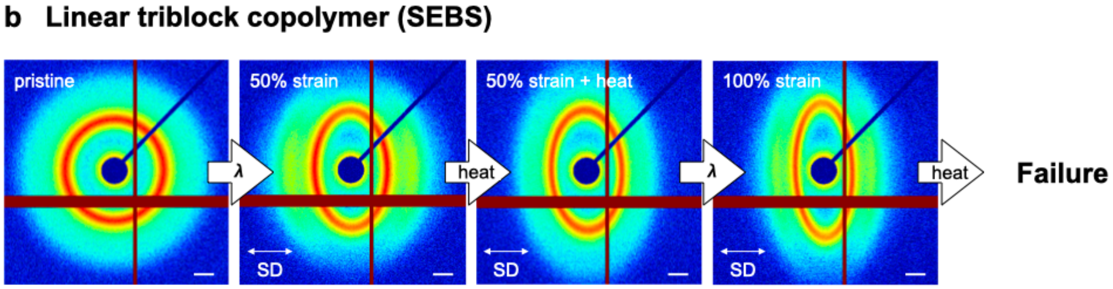

- No domain exchange and network reconstruction at linear polymer
- Rapid failure (~ 100% strain) under thermal stress

Supplementary Fig. 24 | Dynamic exchange of polymer networks under thermal stress. 2D SAXS images of polymer networks during stretching and subsequent heating cycles. **a,** The triblock BBP network exhibits network deformation and dynamic domain exchange even at low strain (50%) under thermal stress, owing to the short contour length of BBPs. The fast exchange dynamics of BBP domains further maintain network integrity under sequential mechanical and thermal stresses. **b,** In contrast, the linear triblock copolymer network does not exhibit network reconstruction at low strain (50%) due to its long contour length. Consequently, the LP network fails at 100% strain due to kinetically trapped linear end blocks. scale bars, 0.02 Å^{-1}.

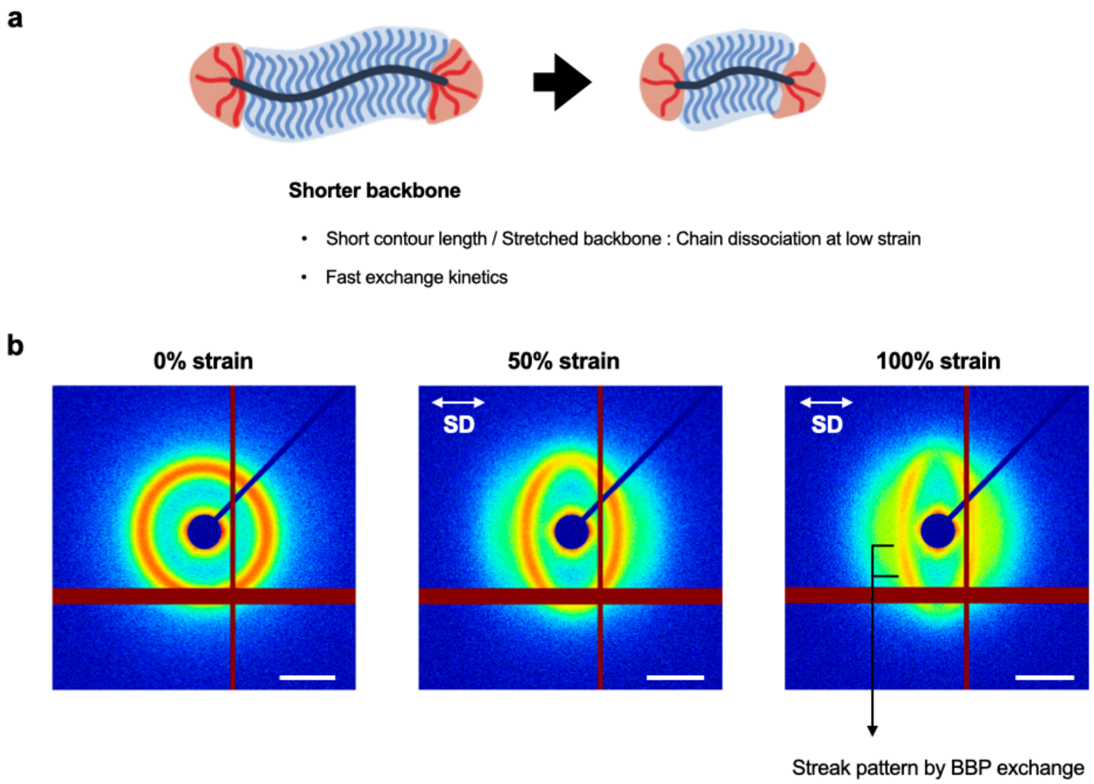

Supplementary Fig. 25 | Network reconstruction of short backbone BBPs. **a,** Effects of backbone length on the exchange dynamics of BBPs. **b,** 2D SAXS images of the short backbone BBP network under uniaxial stretching. Due to their short contour length, the BBPs dissociate from the domains at small strains and rapidly associate with neighboring domains due to their fast chain kinetics. Consequently, domain exchange appeared in the 2D SAXS images even without applying thermal stress. scale bars, 0.02 Å^{-1}.

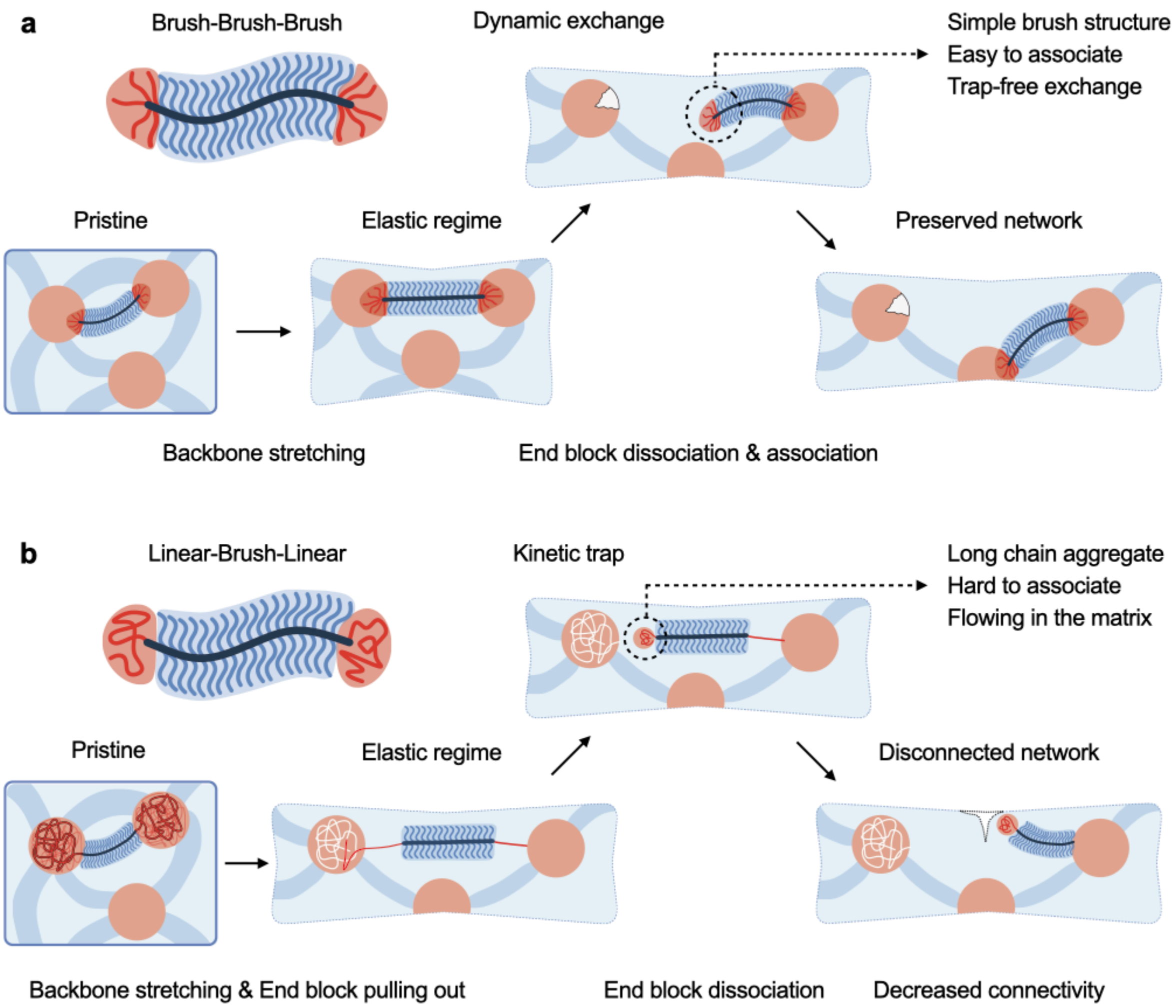

Supplementary Fig. 26 | Different mechanical behavior of BBP and LP end blocks under strain. **a,** Schematic illustration of stretching behavior of a Brush-Brush-Brush (BBB) triblock copolymer. The network shows elastic behavior until the backbone becomes fully stretched. When the BBP end blocks dissociate from their domain at high strain, their intrinsically simple architecture restricts conformational change, so their overall configuration remains unchanged. As a result, brush end blocks rapidly re-associate with other domains, enabling efficient network reconstruction. **b,** Schematic illustration of stretching behavior of a Linear-Brush-Linear (LBL) triblock copolymer. Unlike the brush architecture, the random coil LP end blocks are extracted from the domains before fully dissociating. Once dissociated, the LP blocks tend to aggregate to minimize interfacial area. However, these aggregates cannot re-associate with other domains and flow within the matrix. This aggregation acts as a kinetic trap that hinders network reconstruction, reducing network connectivity and leading to early failure at low strains.

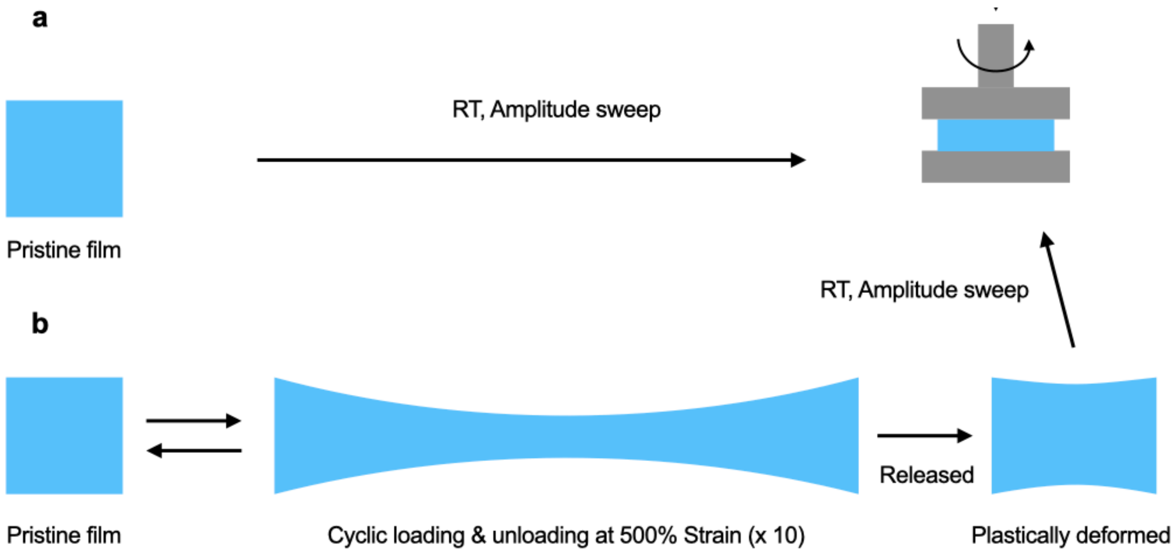

Supplementary Fig. 27 | Validating network connectivity after domain disruption by mechanical stimuli. Schematic illustration of **a,** measuring LVER in pristine elastomer films via rheological amplitude sweep, and **b,** measuring LVER after subjecting films to 10 cycles of 500% strain. After cyclic stretching, plastic deformation reflects partial network disruption. Comparing LVER before and after deformation reveals the fraction of polymer chains that remain effectively connected within the network after domain disruption.

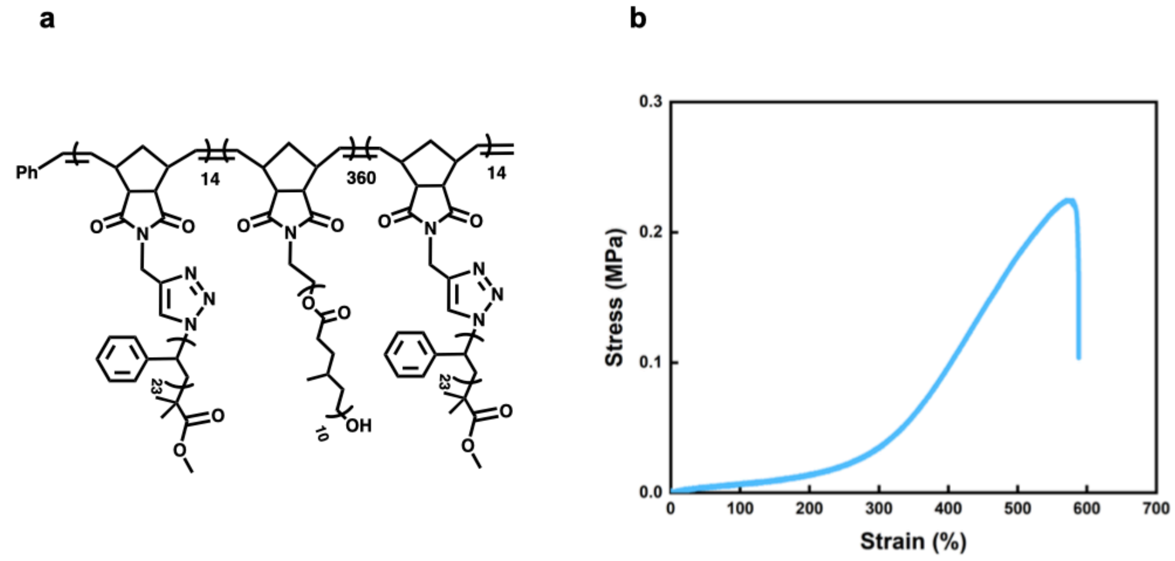

Supplementary Fig. 28 | Validating network connectivity after domain disruption by mechanical stimuli. a, Molecular structure of PS-*b*-P4MCL-*b*-PS triblock BBP. **b,** Uniaxial tensile test result of P4MCL based triblock BBP network. Replacing the middle block side chains with another low T_g polymer leads to similar mechanical responses, indicating that the toughening mechanism is universally applicable.

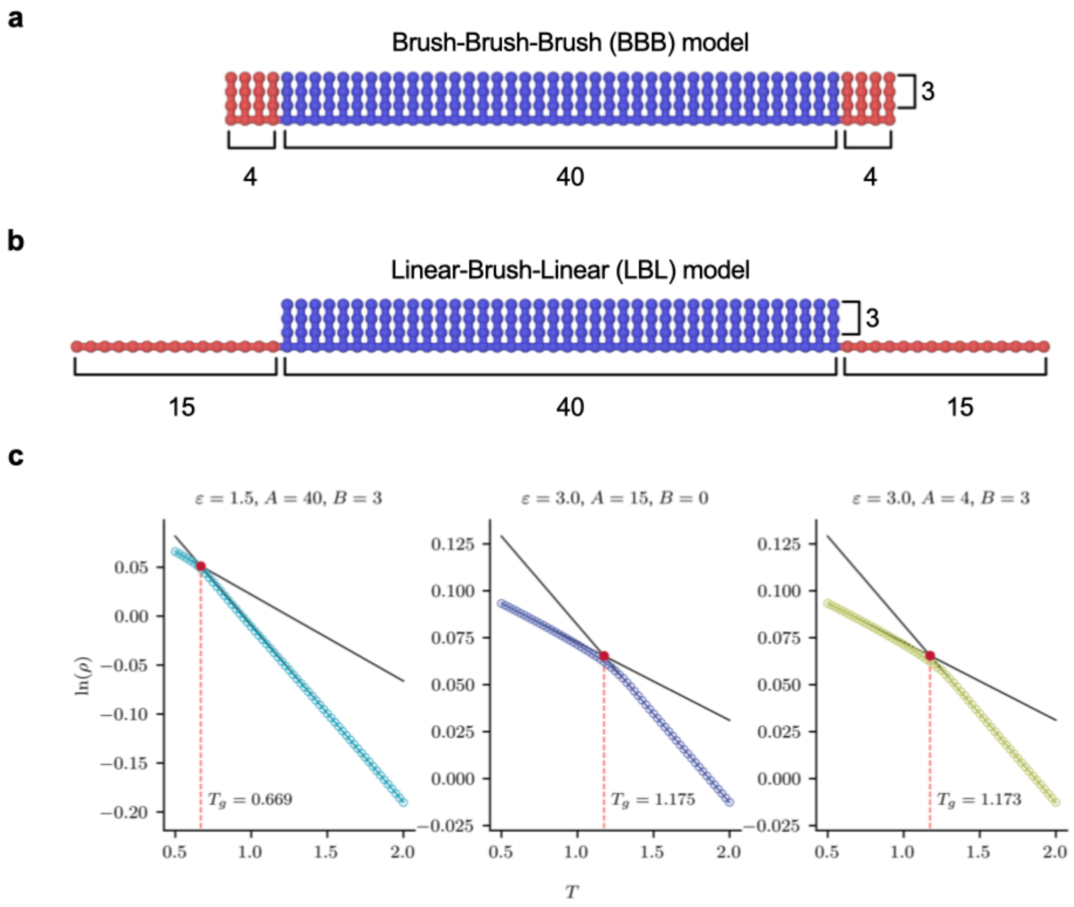

Supplementary Fig. 29 | Model systems for CGMD simulation. Schematic illustrations of **a,** the BBB model and **b,** the LBL model setup. **c,** Glass transition temperature (T_g) of the middle brush block (left), linear end block of LBL model (middle), and brush end block of the BBB model (right). Parameter selection ensures that the middle block is rubbery ($T_g < 1$) while the linear and brush end blocks remain glassy ($T_g > 1$).

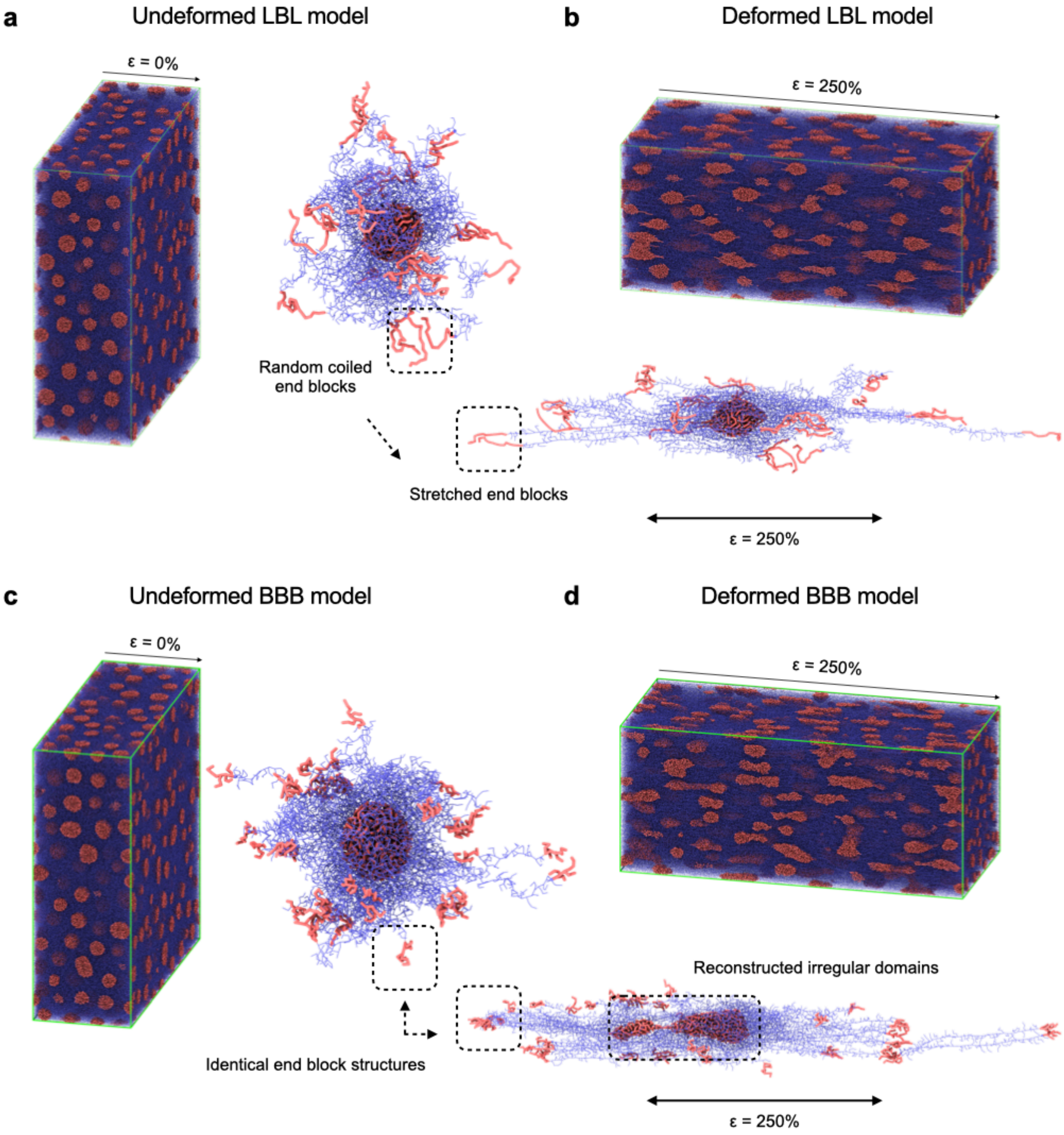

Supplementary Fig. 30 | CGMD simulation of LBL and BBB systems under uniaxial strain. CGMD simulation results of the overall network and domain structures of **a,** the undeformed pristine LBL model, **b,** the LBL model under 250% strain, **c,** the undeformed pristine BBB model, and **d,** the BBB model under 250% strain. Compared to the linear end block system (LBL model), the brush end block system (BBB model) exhibits differences in domain morphology and end block architecture changes upon deformation, resulting from the different structural responses of linear and brush end blocks under applied strain.

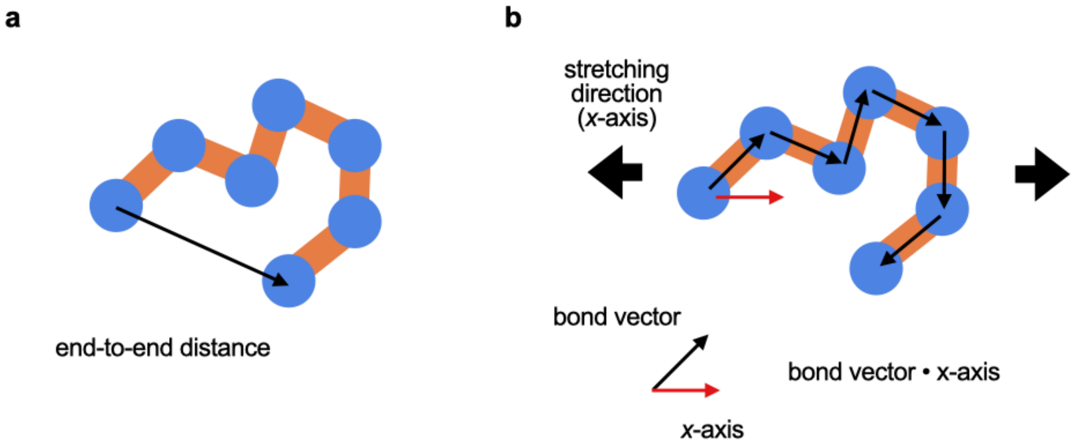

Supplementary Fig. 31 | Structural parameters in CGMD simulation. **a,** Schematic illustration of normalized squared end-to-end distance. Monitoring this parameter during stretching enables tracking of conformational changes of each block. **b,** Schematic illustration of backbone nematic order parameter used to evaluate chain conformation and orientation. The parameter quantifies the alignment of polymer backbones relative to the applied strain, reflecting the fraction of the chains that bear the applied load.

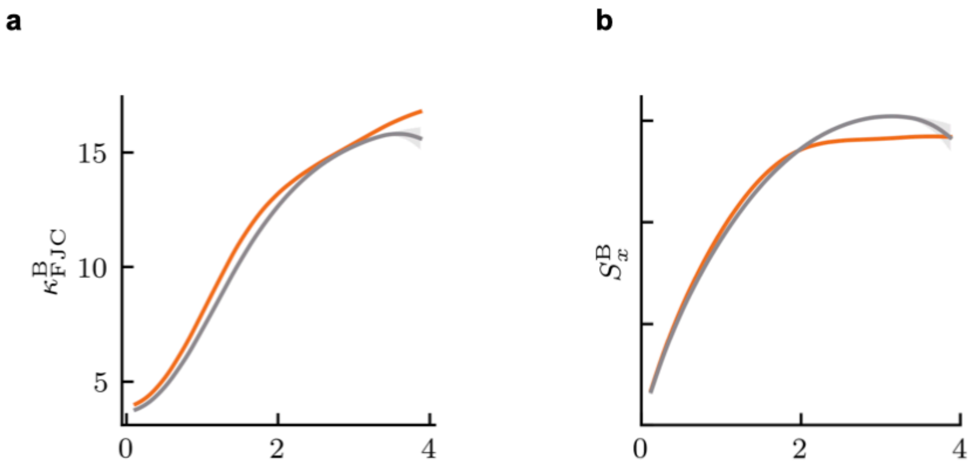

Supplementary Fig. 32 | Structural parameter of brush middle block under uniaxial stretching. a, Normalized end-to-end distance and **b,** nematic order parameter of the middle brush block in both BBB and LBL systems. The two systems exhibit nearly identical behavior for the middle block under stretch.

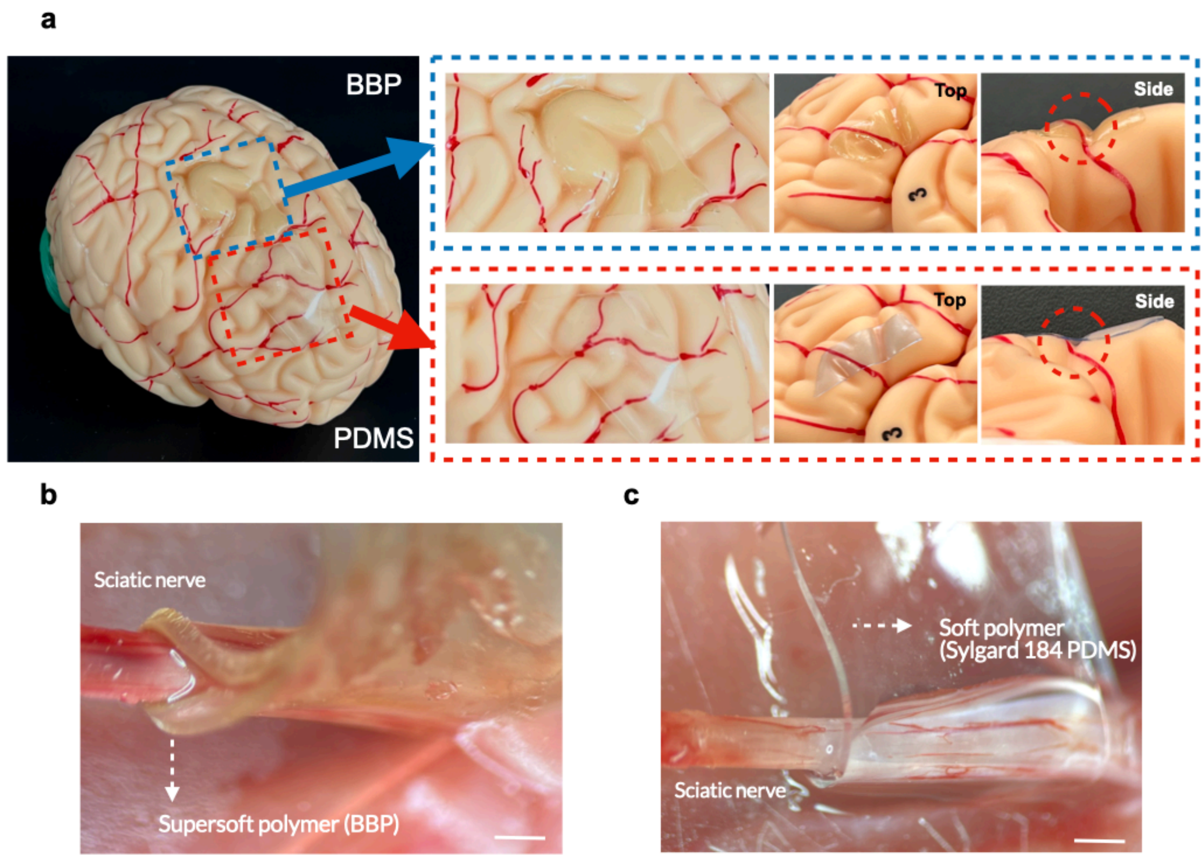

Supplementary Fig. 33 | Conformal contact of triblock BBP films. a, Photographs of BBP and PDMS films placed on a wavy brain-mimicking surface. **b,** Conformal wrapping of BBP films as a cuff substrate around a thin fiber-like structure (sciatic nerve). **c,** Large gap formed between nerve and PDMS substrate. Owing to their supersoft nature, BBP films conformally adhere to curved surfaces without gaps, whereas PDMS—although soft—fail to achieve conformal contact on highly curved geometries.

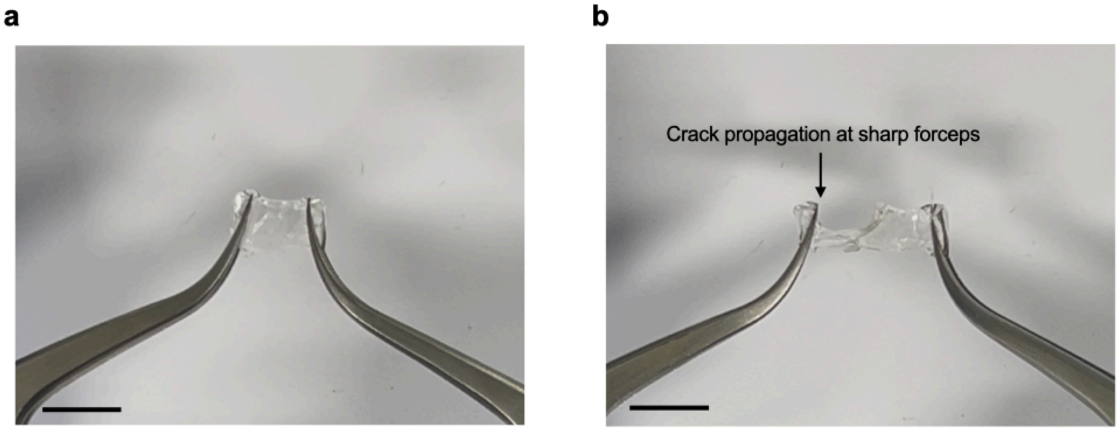

Supplementary Fig. 34 | Low toughness and poor fracture resistance of chemically crosslinked BBP networks. a, Photographs of a chemically crosslinked BBP network before and stretching **b,** Photographs of the same network after stretching with surgical forceps. Owing to insufficient mechanical resilience, previously reported supersoft BBP networks fracture readily under gentle handling, limiting their suitability for implantable applications. Scale bars, 1 cm.

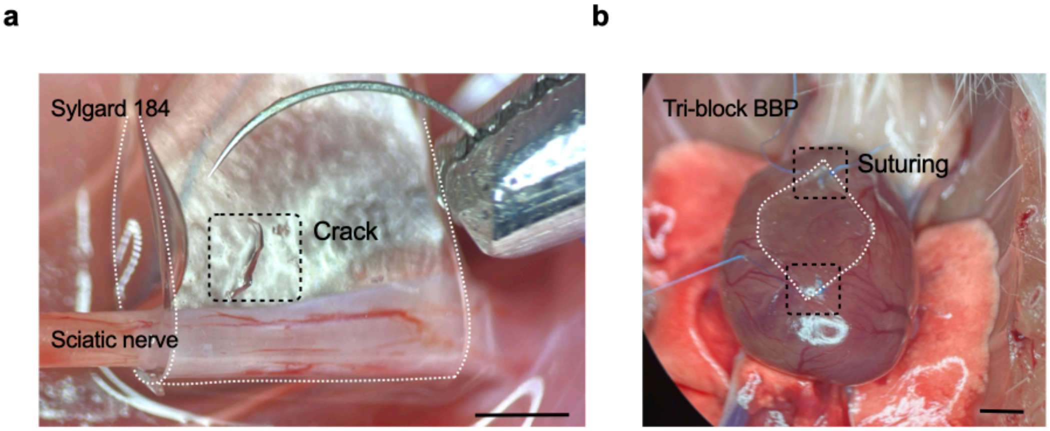

Supplementary Fig. 35 | Effects of crack resistance on suturing of bioimplants. a, Photographs of suturing Sylgard 184 substrate for cuff fixation **b,** Photographs of suturing a triblock BBP substrate onto a rat heart. Sylgard 184 is not suturable owing to its high crack sensitivity, whereas the BBP network, with exceptional crack resistance, can be sutured onto dynamically moving tissues such as the heart while maintains conformal contact. Scale bars, 2 mm.

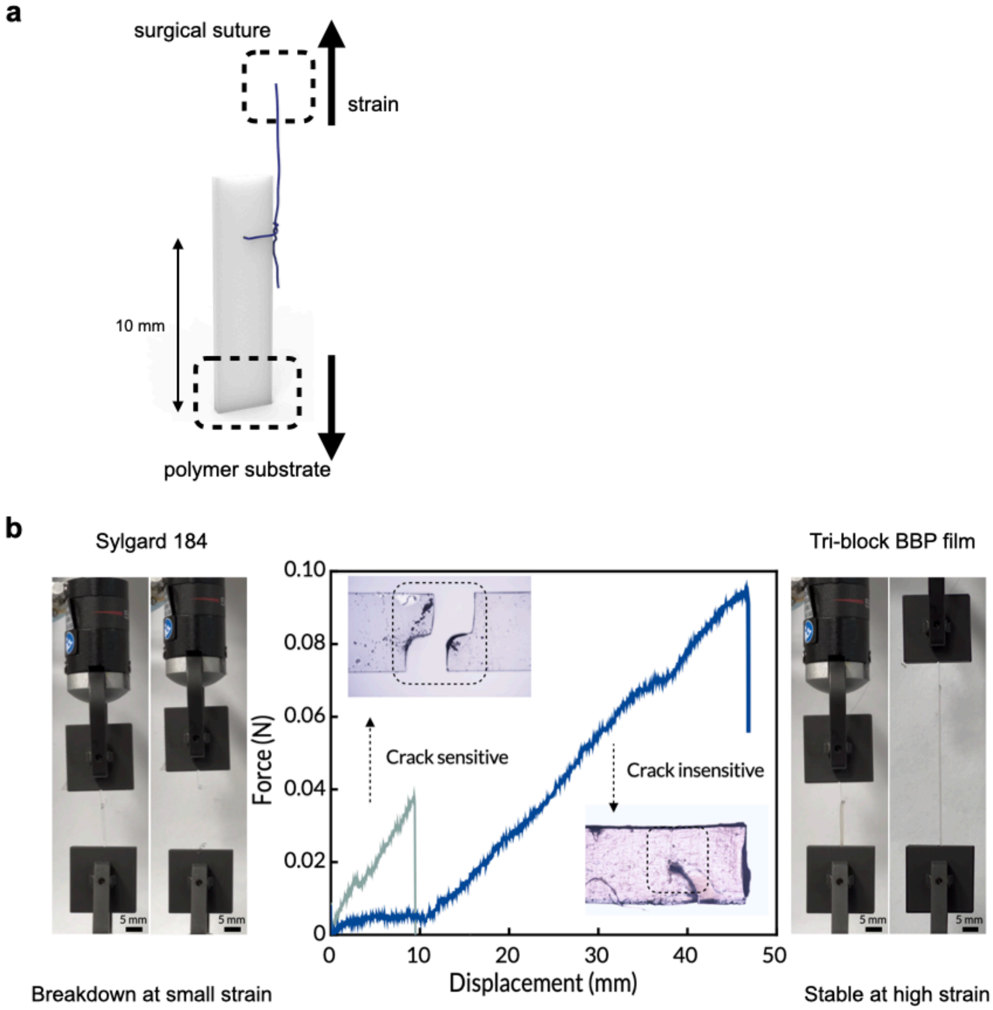

Supplementary Fig. 36 | Suturable supersoft elastomer. a, Schematic of the force measurement setup between a surgical suture and the substrate. **b,** Photographs and force-strain curves for PDMS (Sylgard 184) and triblock BBP films. The high crack sensitivity of PDMS causes a sharp rise in force with strain, leading to immediate failure at the notch. In contrast, the BBP substrate's supersoft and tough nature enables stress deconcentration, allowing it to stretch under low force and sustain substantially higher strain and load without fracture.

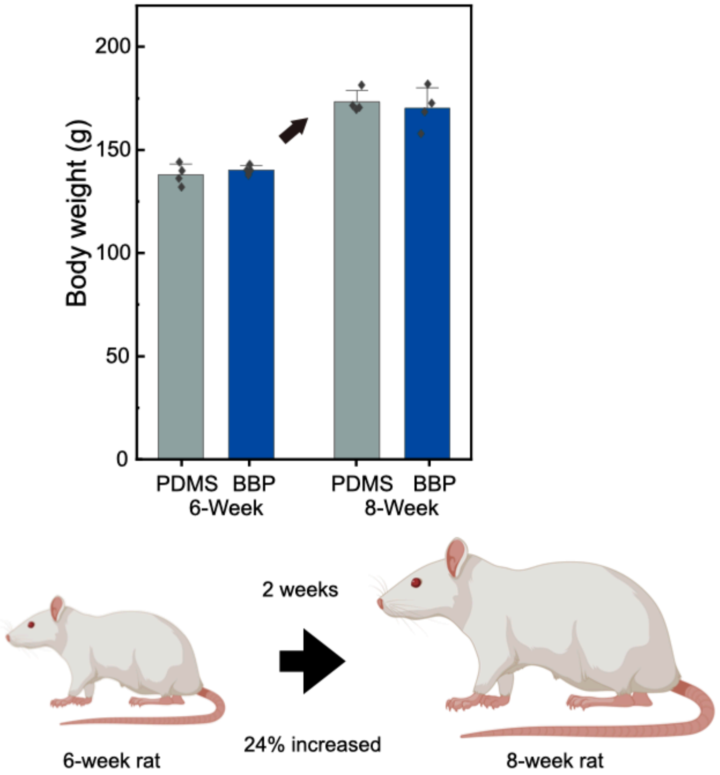

Supplementary Fig. 37 | Body weight changes during implantation period. Six-week-old rats implanted with intraneural mock devices continued to grow, gaining an average of 24% in body weight over the 2-week implantation period. This body growth imposed continuous mechanical tension and compression on the implanted devices due to tissue expansion.

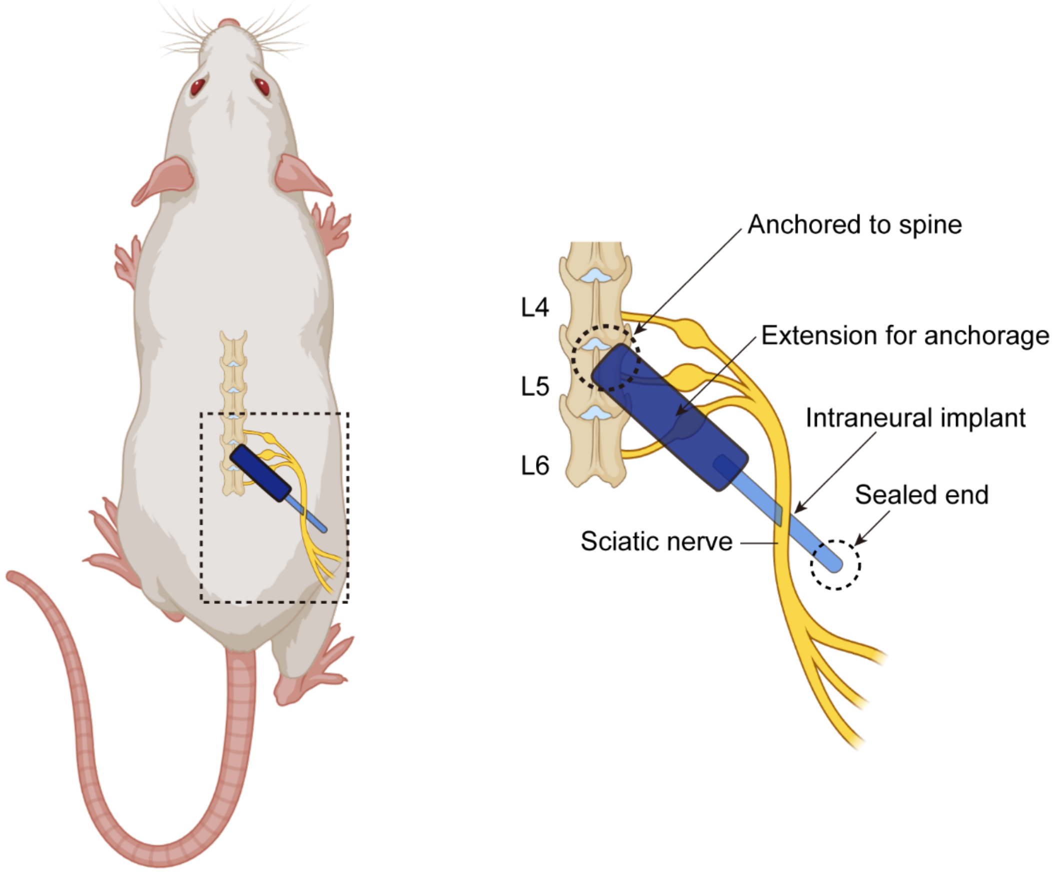

Supplementary Fig. 38 | System of the intraneural implant. Schematic illustration of the intraneural device targeting the peripheral nerve. The proximal end is connected to a PDMS connector and anchored to the L4-L5 Vertebrae using Super-Bond and dental cement, while the distal end is sealed with Kwik-Sil to prevent dislocation. Because the implant is anchored to the spine, body movement continuously imposes tensile and torsional stresses on the device.

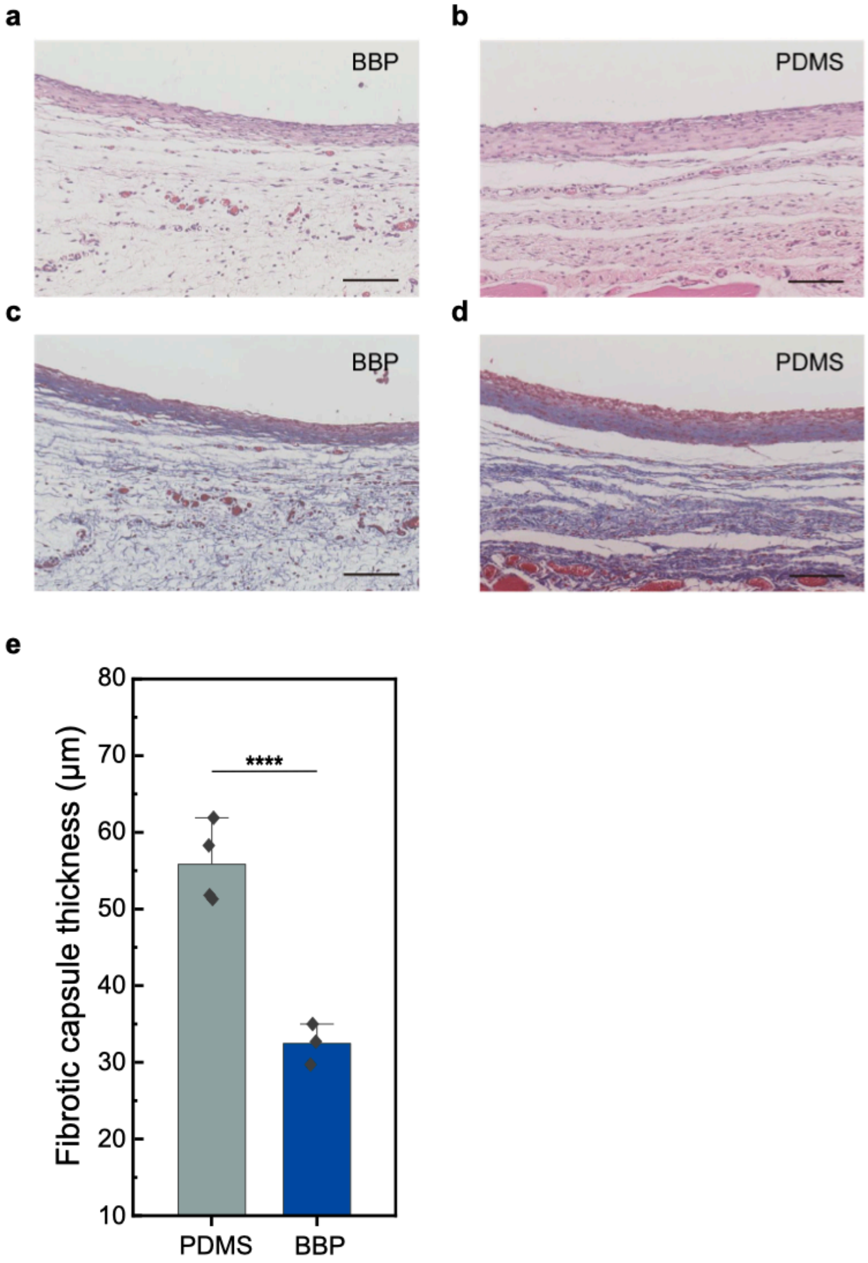

Supplementary Fig. 39 | Histological analyses of supersoft polymers to assess foreign body response at 2-week post-implantation in rat subcutaneous dorsal pocket. Hematoxylin and Eosin staining of tissue sections after implantation of **a,** BBP and **b,** PDMS films. Masson's trichrome staining of tissue sections after sections after implantation of **c,** BBP and **d,** PDMS films. Scale bars, 100 µm. **e,** Quantitative analysis of fibrotic capsule formation following implantation of BBP and PDMS films (n = 3 animals, P = 0.00088). Statistical significance and P value is determined by two-sided unpaired t-test (****P ≤ 0.0001).

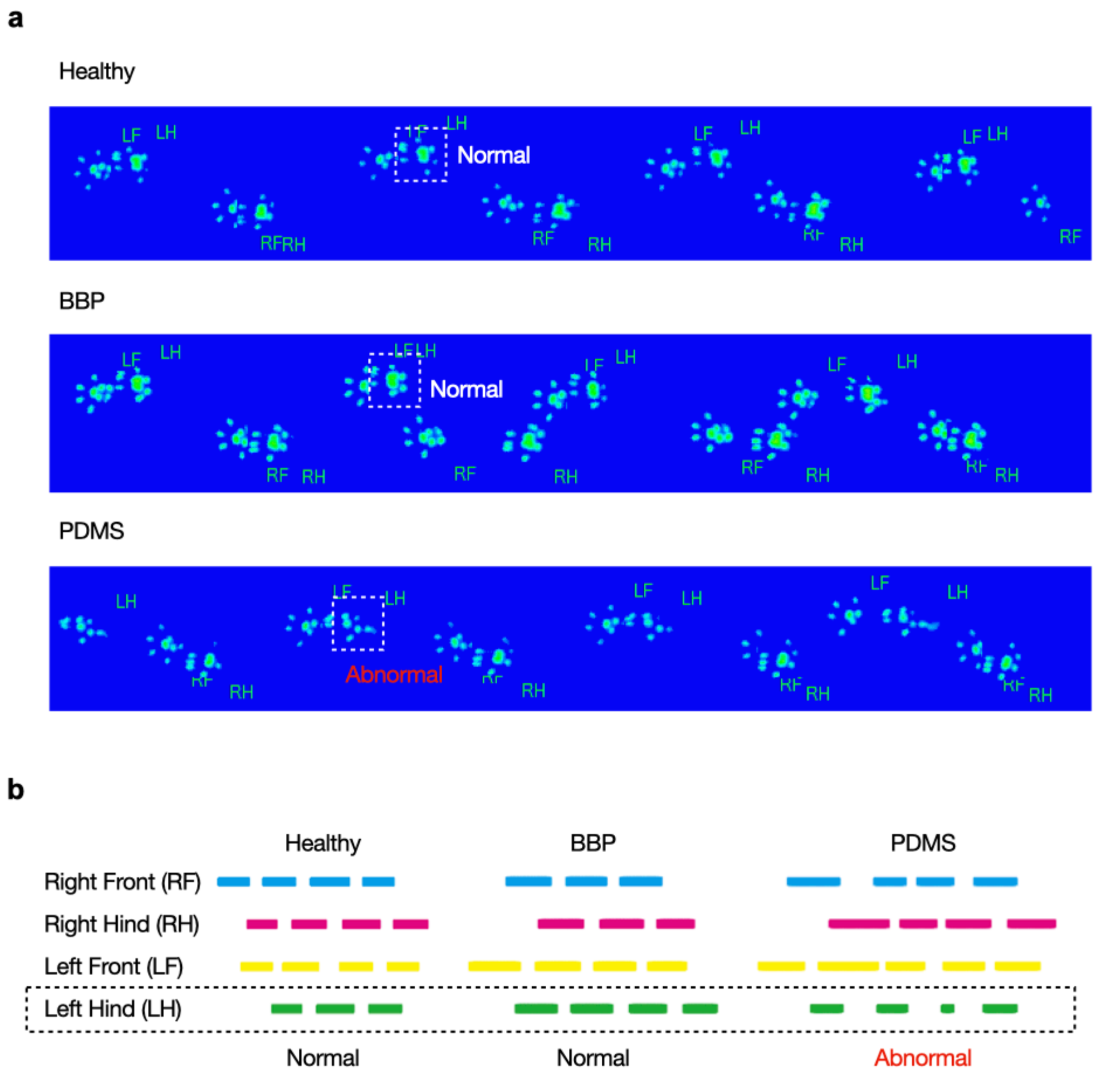

Supplementary Fig. 40 | Gait and walking analysis. a, Representative gait images and **b,** walking trajectories of the three experimental groups. The BBP-implanted group exhibits normal gait and walking behavior comparable to healthy controls, whereas the PDMS-implanted group shows abnormal gait and irregular steps due to sciatic nerve injury.

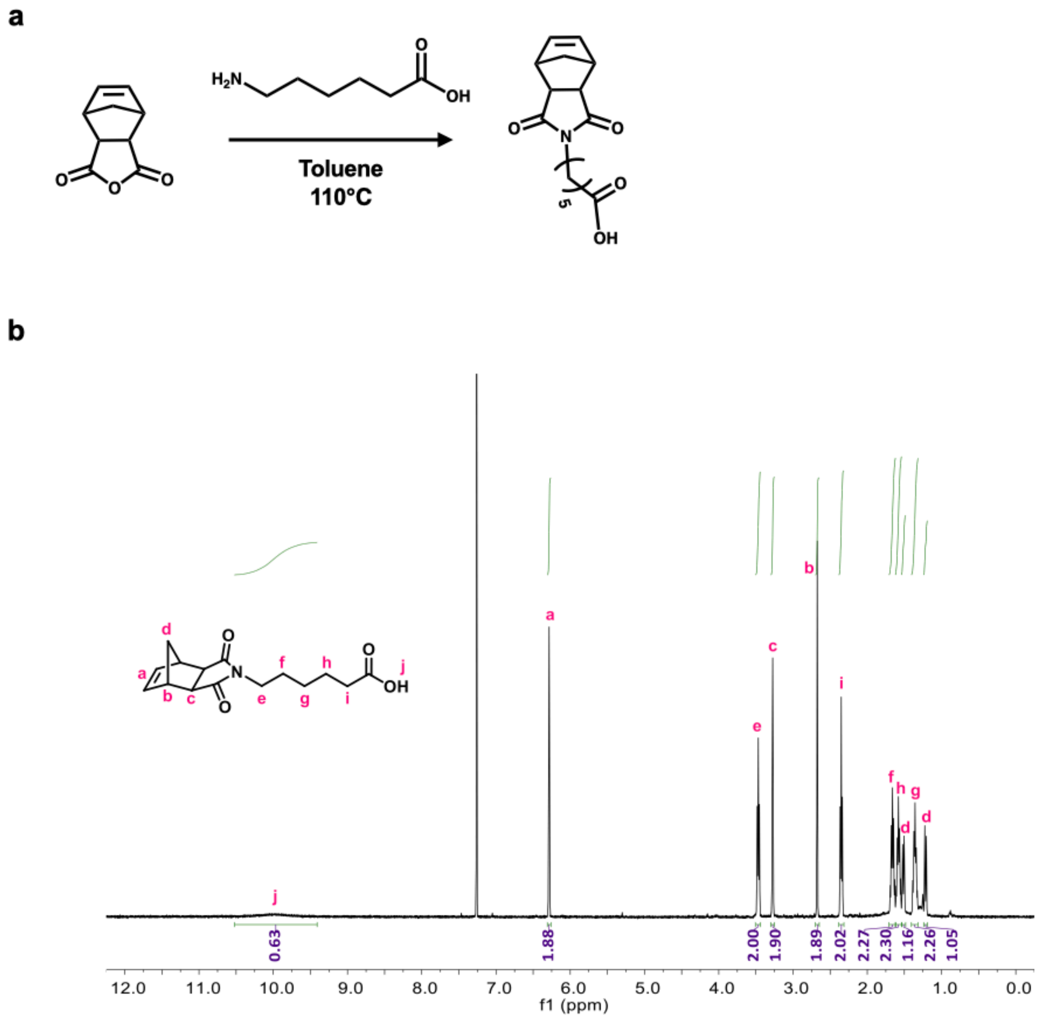

Supplementary Fig. 41 | Synthesis of Nb-COOH. a, Synthetic scheme and **b,** ^{1}H NMR spectrum of Nb-COOH measured in $CDCl_3$ (500 MHz).

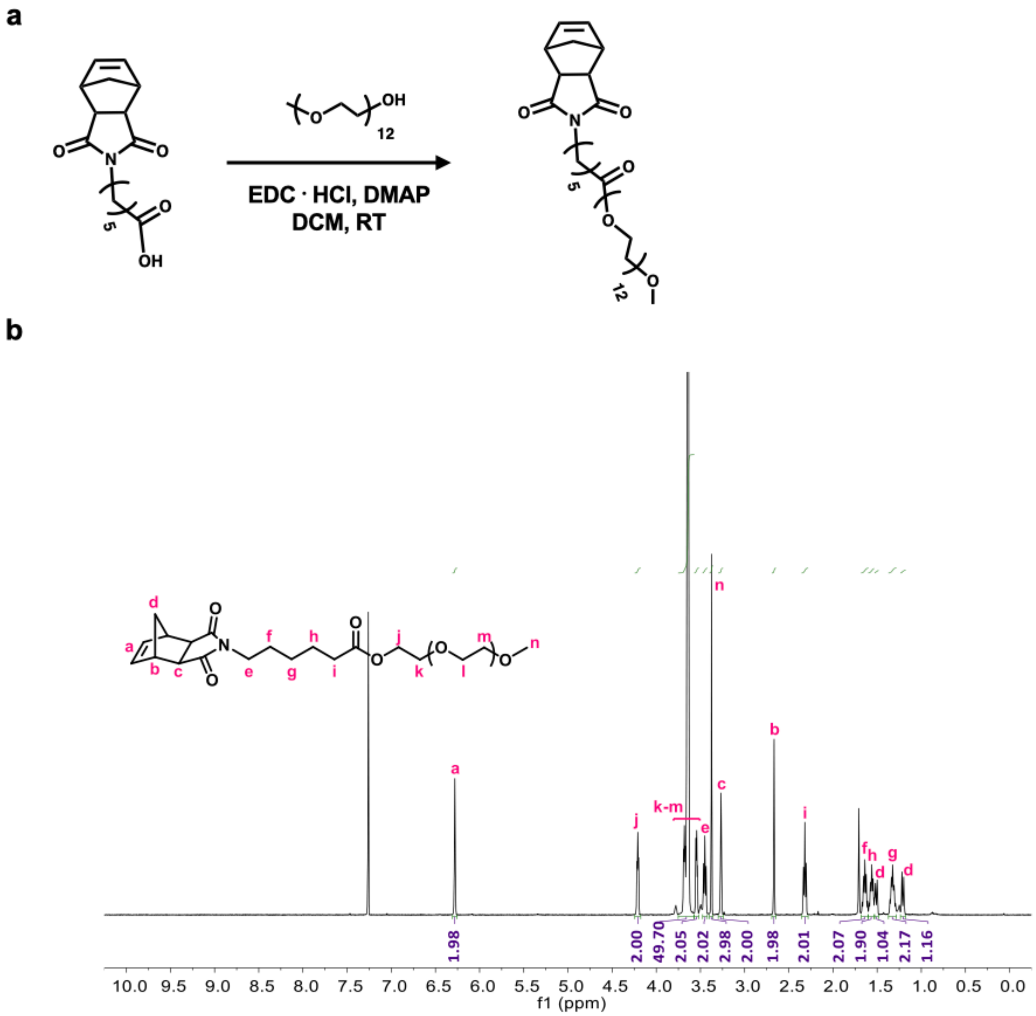

Supplementary Fig. 42 | Synthesis of Nb-PEG macromonomer. a, Synthetic scheme and **b,** ^{1}H NMR spectrum of Nb-PEG macromonomer measured in $CDCl_3$ (500 MHz).

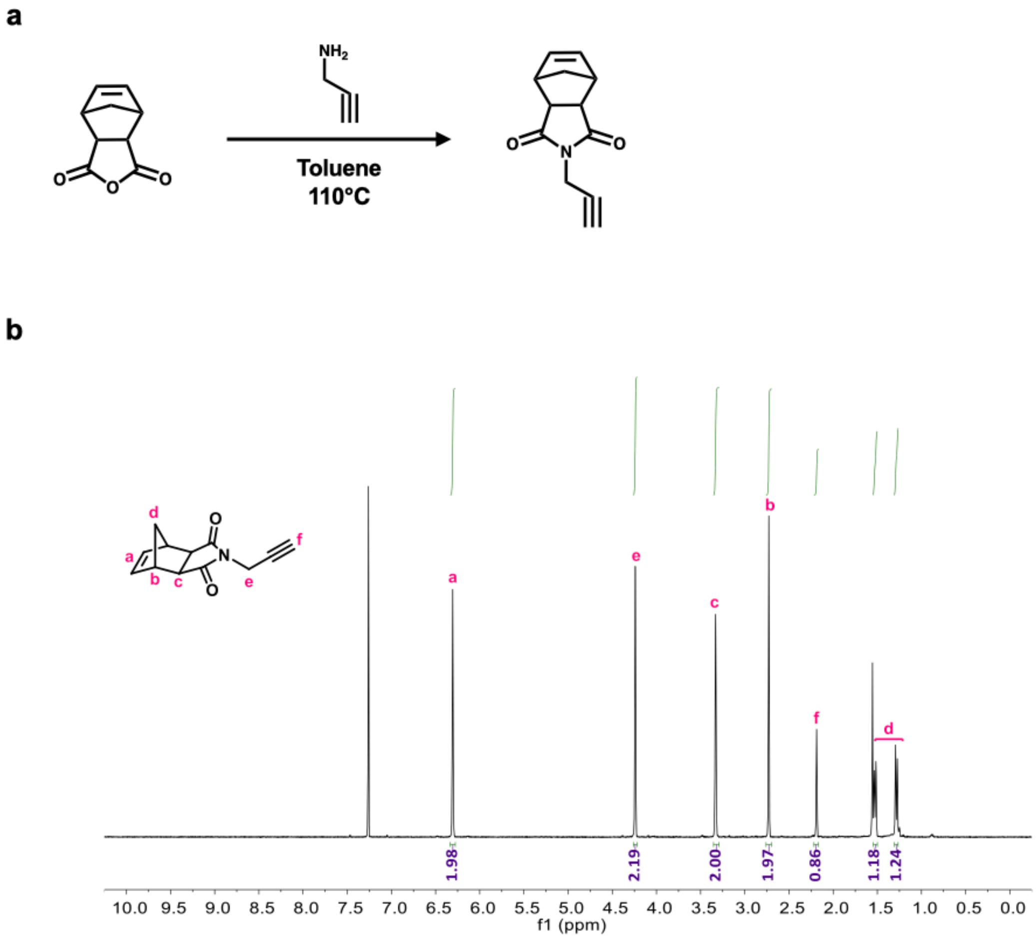

Supplementary Fig. 43 | Synthesis of Nb-propargyl imide. a, Synthetic scheme and **b,** ^{1}H NMR spectrum of Nb-propargyl amide measured in $CDCl_3$ (500 MHz).

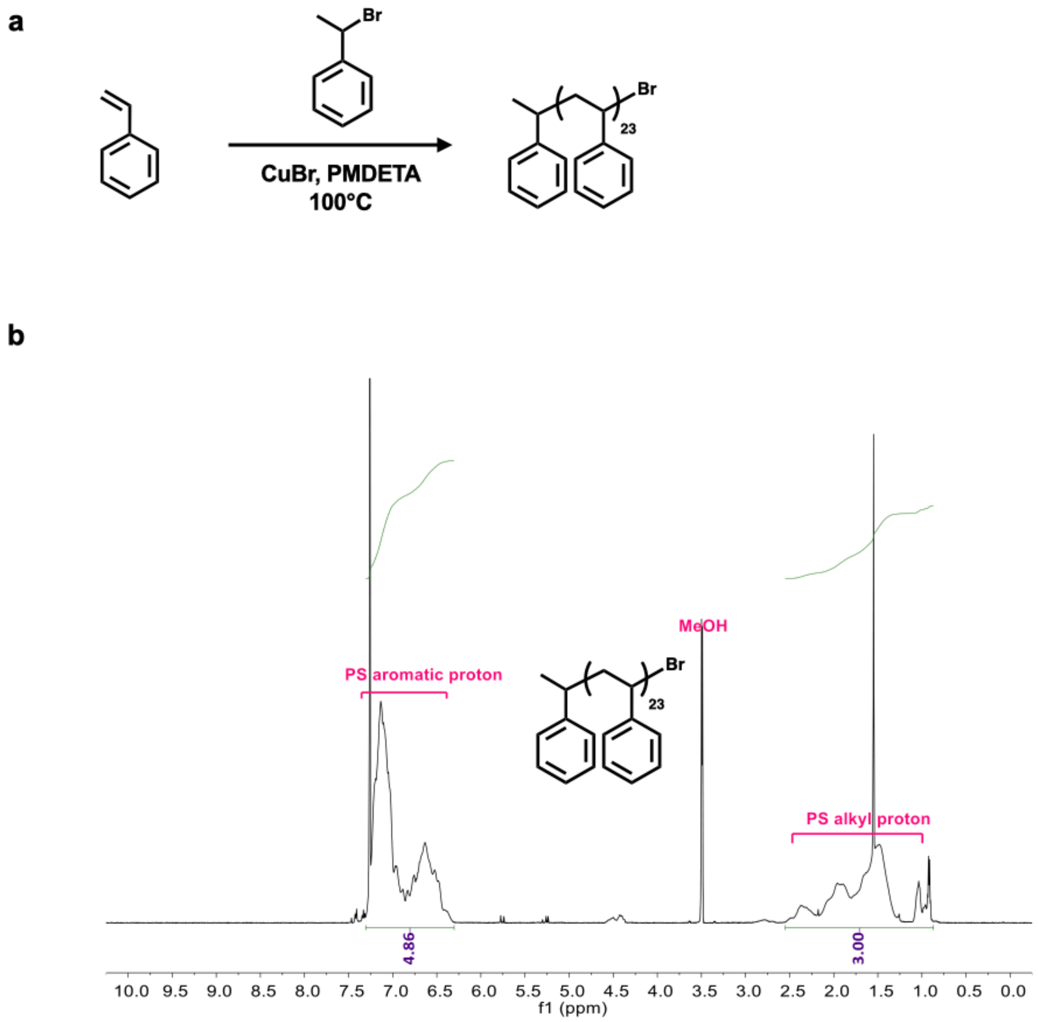

Supplementary Fig. 44 | Synthesis of PS-Br. a, Synthetic scheme and **b,** ^{1}H NMR spectrum of PS-Br measured in $CDCl_3$ (500 MHz).

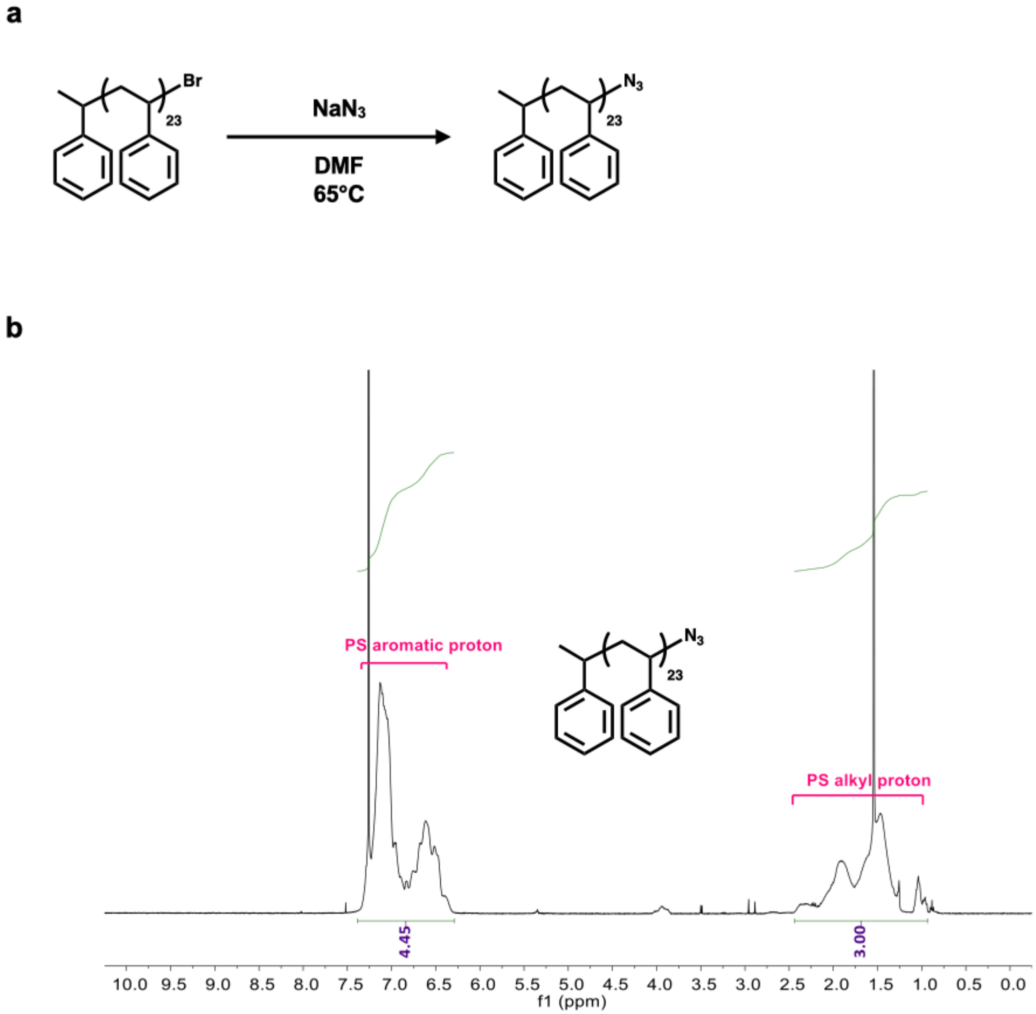

Supplementary Fig. 45 | Synthesis of PS-N$_3$. a, Synthetic scheme and **b,** ^{1}H NMR spectrum of PS-N$_3$ measured in CDCl$_3$ (500 MHz).

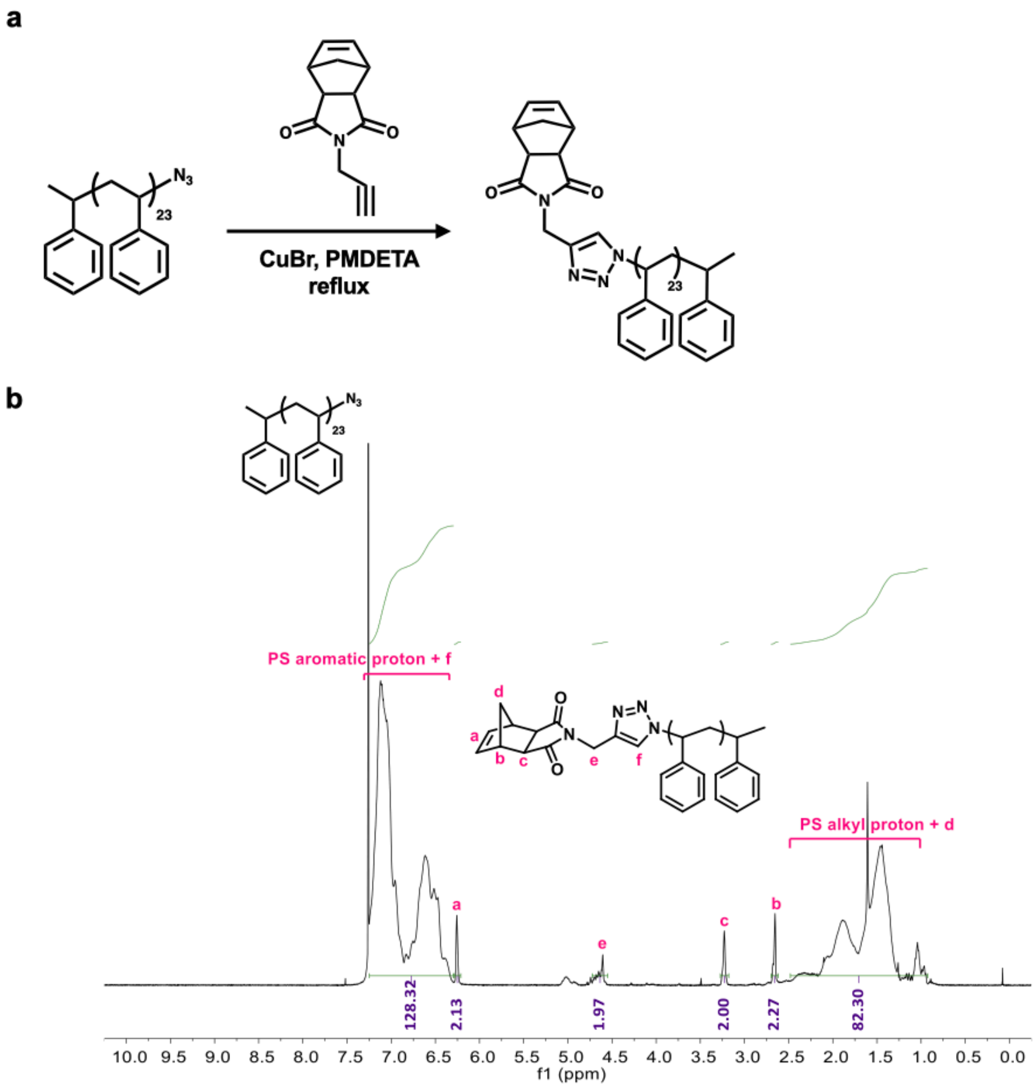

Supplementary Fig. 46 | Synthesis of Nb-PS macromonomer. a, Synthetic scheme and **b,** ^{1}H NMR spectrum of Nb-PS macromonomer measured in $CDCl_3$ (500 MHz).

Supplementary Table

Sample	PS MW / $N_{\text{bb, single block}}$	PEG MW / N_{bb}	Calculated PS vol% (d_{PS} = 1.00 / d_{PEG} = 1.15)	Young's modulus (MPa)	Maximum strain (%)	Maximum stress (MPa)
PS homo brush	2.5 k / 300	-	100	Brittle solid		
PEG homo brush	-	0.1 k / 300	0	0.2	880 (viscoelastic)	0.06
	-	0.5 k / 300	0	Viscous liquid		
	-	4.0 k / 300	0	Brittle solid		
PS-*b*-PEG-*b*-PS triblock brush	2.5 k / 6	0.5 k / 180	20	0.13	360	0.52
	2.5 k / 24	0.5 k / 720	20	0.03	1,140	0.53
	2.5 k / 6	0.5 k / 360	11	0.04	530	0.40
	2.5 k / 12	0.5 k / 360	20	0.04	1,260	1.32
	2.5 k / 18	0.5 k / 360	28	0.13	1,260	2.43
	2.5 k / 24	0.5 k / 360	34	0.70	1,180	5.23
	2.5 k / 36	0.5 k / 360	43	3.0	850	7.85
	2.5 k / 48	0.5 k / 360	50	35.0	460	8.00

Supplementary Table 1 | Summary of synthesized BBPs and the mechanical properties.

Supplementary Video

Supplementary Video 1 | On demand suturing of BBP on dynamically beating rat heart. The high fracture toughness of the triblock BBP substrate enables on demand suturing without the risk of device failure. Suturing ensures high conformality for long-term operation on dynamically deforming tissues, such as the heart.

Supplementary references

1. Liu, D. *et al.* Tubulation repair mitigates misdirection of regenerating motor axons across a sciatic nerve gap in rats. *Sci. Rep.* **8**, 3443 (2018).
2. Martínez-Carranza, M. *et al.* Activity of botulinum neurotoxin X and its structure when shielded by a non-toxic non-hemagglutinin protein. *Commun. Chem.* **7**, 179 (2024).
3. Bozkurt, A. *et al.* CatWalk gait analysis in assessment of functional recovery after sciatic nerve injury. *Journal of Neuroscience Methods* **173**, 91–98 (2008).
4. Varejão, A. S. P., Melo-Pinto, P., Meek, M. F., Filipe, V. M. & Bulas-Cruz, J. Methods for the experimental functional assessment of rat sciatic nerve regeneration. *Neurol. Res.* **26**, 186–194 (2004).
5. Bain, J. R., Mackinnon, S. E. & Hunter, D. A. Functional Evaluation of Complete Sciatic, Peroneal, and Posterior Tibial Nerve Lesions in the Rat: *Plast. Reconstr. Surg.* **83**, 129–136 (1989).
6. Marcolino, A. M. *et al.* Assessment of Functional Recovery of Sciatic Nerve in Rats Submitted to Low-Level Laser Therapy with Different Fluences. An Experimental Study. *J. Hand Microsurg.* **5**, 49–53 (2013).
7. Zheng, G. *et al.* Assessment of hindlimb motor recovery after severe thoracic spinal cord injury in rats: classification of CatWalk XT® gait analysis parameters. *Neural. Regen. Res.* **18**, 1084 (2023).
8. Li, T., Senesi, A. J. & Lee, B. Small Angle X-ray Scattering for Nanoparticle Research. *Chem. Rev.* **116**, 11128–11180 (2016).
9. Lin, T.-P. *et al.* Effects of Grafting Density on Block Polymer Self-Assembly: From Linear to Bottlebrush. *ACS Nano* **11**, 11632–11641 (2017).

10. Vatankhah-Varnosfaderani, M. *et al.* Mimicking biological stress–strain behaviour with synthetic elastomers. *Nature* **549**, 497–501 (2017).

11. Li, X. & Gong, J. P. Design principles for strong and tough hydrogels. *Nat. Rev. Mater.* **9**, 380–398 (2024).

12. Gong, J. P., Katsuyama, Y., Kurokawa, T. & Osada, Y. Double-Network Hydrogels with Extremely High Mechanical Strength. *Adv. Mater.* **15**, 1155–1158 (2003).

13. Sun, J.-Y. *et al.* Highly stretchable and tough hydrogels. *Nature* **489**, 133–136 (2012).

14. Liu, C. *et al.* Tough hydrogels with rapid self-reinforcement. *Science* **372**, 1078–1081 (2021).

15. Kim, J., Zhang, G., Shi, M. & Suo, Z. Fracture, fatigue, and friction of polymers in which entanglements greatly outnumber cross-links. *Science* **374**, 212–216 (2021).